This paper appears in IEEE Transactions on Automation Science and Engineering, 2025.
https://doi.org/10.1109/TASE.2025.3540860

Trajectory Tracking Control of Wheeled Mobile Manipulators with Joint Flexibility via Virtual Decomposition Approach

Hongjun Xing, *Member, IEEE*, Yuzhe Xu, Liang Ding, *Senior Member, IEEE*, Jinbao Chen, Haibo Gao, and Mahdi Tavakoli, *Senior Member, IEEE*

***Abstract*—Wheeled mobile manipulators (WMMs) involving a wheeled mobile platform and a serial manipulator are finding increasing applications in diverse fields, creating new challenges in performing high-precision operations in a spacious workspace. WMMs are challenging to control due to uncertainties in system parameters, coupled dynamics, and external disturbances, which make stability guarantees difficult. This paper proposes a virtual decomposition control (VDC)-based trajectory tracking controller for WMMs, addressing joint flexibility, external disturbances, etc. The proposed method uses a VDC-based iterative approach to manage the complex coupled dynamics and employs a separate adaptive controller to handle joint flexibility. The robotic system's stability is validated using the specific features of VDC (proof of each subsystem's *virtual stability*) according to the Lyapunov stability theory. The advantages and effectiveness of the proposed method are demonstrated through experiments.**

***Note to Practitioners*—This paper addresses the challenges faced in controlling WMMs, which are becoming increasingly common in various industrial and service applications due to their ability to perform tasks in large and dynamic environments. The coupling between the wheeled platform and the manipulator, as well as uncertainties in system parameters such as joint flexibility and external disturbances, make precise trajectory tracking difficult. To address these challenges, this paper presents a control approach based on VDC, which breaks down the complex system into manageable subsystems and ensures stability for each part individually. The control strategy also incorporates adaptive control to handle joint flexibility and unpredictable disturbances. The stability of the system is rigorously proven through Lyapunov theory, ensuring robust performance under real-world conditions. Practitioners working on autonomous mobile robots equipped with manipulators may find this approach useful for improving trajectory tracking performance in uncertain and dynamic environments. However, the practical implementation of this method will require careful tuning of controller parameters and real-time computational capabilities to ensure seamless operation in real applications.**

This work was supported by the National Natural Science Foundation of China (Grant No. 52405025), the Natural Science Foundation of Jiangsu Province (Grant No. BK20230889), State Key Laboratory of Robotics and Systems (HIT) (Grant No. SKLRS-2023-KF-04), Canada Foundation for Innovation (CFI), and the Natural Sciences and Engineering Research Council (NSERC) of Canada. (H. Xing is the corresponding author).

H. Xing, Y. Xu, and J. Chen are with the National Key Laboratory of Aerospace Mechanism, Nanjing University of Aeronautics and Astronautics, Nanjing 210016, China. (e-mails: {xinghj, xuyuzhe, chenjbao}@nuaa.edu.cn).

L. Ding and H. Gao are with the State Key Laboratory of Robotics and System, Harbin Institute of Technology, Harbin 150001, China. (e-mails: {liangding, gaohaibo}@hit.edu.cn).

M. Tavakoli is with the Department of Electrical and Computer Engineering, University of Alberta, Edmonton T6G 1H9, Alberta, Canada. (e-mail: mahdi.tavakoli@ualberta.ca).

***Index Terms*—Wheeled mobile manipulator, Coupled dynamics, Trajectory tracking, Virtual decomposition control, Stability analysis.**

I. Introduction

Wheeled mobile manipulators (WMMs) are gaining popularity for applications such as planetary exploration, disaster rescue, and construction/service tasks due to their superior mobility and operational capabilities [1]–[4]. A key component of the above-mentioned applications is the robot's accurate trajectory tracking performance. Even though many powerful modeling approaches (Lagrangian method [5], Newton–Euler method [6], Kane's approach [7]) and many advantageous control theories (robust control [8], neural networks [9]) have been developed, it remains challenging for researchers and scholars to design a practical and efficient tracking controller for WMMs due to the complex coupled dynamics, uncertainties in the system, and external disturbances. Besides, the robotic system's stability and tracking convergence with environmental disturbances should be guaranteed because the contact dynamics can be severe if the robot dynamics are not treated adequately [10].

Two fundamental approaches to kinematic modeling for WMMs have been employed in many studies. Several authors have added constraints imposed by a mobile base directly to the manipulator model, focusing on decoupling the control of the mobile platform and manipulator. However, these methods fail to fully control the entire WMM system with a single controller, leading to suboptimal performance in complex environments [11]. Picard *et al.* [12] established the models and control laws for the two subsystems, respectively, and designed a coordination paradigm to face the variety of tasks to be achieved. A different approach explicitly formulates the admissible motions in relation to the platform constraints [13], which considers the WMM as a single system, with a dynamic interaction between the platform and the manipulator. Chen *et al.* [14] reported on a matrix transformation-based kinematic model for a four-wheeled holonomic mobile manipulator, coupled with a redundancy resolution approach to maximize the WMM's manipulability. Xing *et al.* [15] focused on improving the motion accuracy of WMMs through a kinematics-based approach that leverages the system's redundancy.

Robot dynamics also play a significant role in achieving high operation performance along with kinematics. With a more accurate dynamic model, the system will be able to move more accurately, as well as respond faster to changes in the external environment. Nader *et al.* [16] built kinematic and dynamic modeling for a WMM using Newton–Euler method, and explained how its end-effector (EE) could track a desired trajectory while controlling the platform's motion over irregular ground surfaces. However, the simulated manipulator only had two degrees of freedom (DoFs) and no joint dynamics were considered. Padois *et al.* [5] established a WMM dynamic model using Lagrangian method to deal with complex robotic missions. However, the Lagrangian method will contain Lagrange multipliers when nonholonomic constraints are involved, which cannot be eliminated until the WMM's motion equation is obtained. To avoid introducing Lagrange multipliers, Tanner and Kyriakopouos [17] proposed to built WMMs' dynamic model using Kane's approach, yet no experimental verification was performed. In addition, fuzzy logic, neural networks, and machine learning-based approach have been widely used in the field of robot modeling and control as tools for system estimation or approximation [18]–[21]. However, these model-free approaches do not explicitly consider system dynamics and are challenging to implement to predict future outcomes.

The flexibility of the joints contributes significantly to the dynamic control of a WMM-mounted manipulator. Ghorbel *et al.* [22] assumed that there was weak joint elasticity in a flexible manipulator and presented the first adaptive control approach for it. Fateh [23] presented a novel uncertainty estimation approach to develop a robust tracking controller for flexible joint manipulators. However, only simulation verification was provided. It was reported in Ma *et al.* [24] that flexible-joint manipulators could benefit from an adaptive fuzzy control strategy, where a fuzzy-logic algorithm was used to resolve the nonlinearity. Despite this, this approach was applicable only to single-link manipulators, and real-time implementations were not attempted. Ding *et al.* [25] presented a separate adaptive controller for the joints of a flexible manipulator, which decoupled the control of the joints and the links. In addition, several model-free methods have been proposed for manipulators with flexible joints [26]–[28].

In general, the trajectory tracking approaches of complex WMM systems can be divided into decentralized control and centralized control. Du *et al.* [29] proposed a dynamic event-triggered fuzzy control approach for multi-agent systems with parameter uncertainties, achieving efficient and robust trajectory tracking control in manipulator-related systems. Papadopoulos and Poulakakis [30] virtually divided a mobile manipulator into a holonomic manipulator subsystem and a nonholonomic mobile platform (MP) subsystem and designed controllers for each, with system dynamic couplings treated as external disturbances. Fareh *et al.* [31] presented a decentralized control method for a mobile manipulator, where the controllers of the MP and the manipulator are separately designed, and with the consideration of the subsystems' coupling, the global stability of the closed-loop system was proved using the Lyapunov approach. However, joint friction and nonlinearities were not considered. An approach developed by Yamamoto and Yun [32] compensated the dynamic coupling of mobile manipulators by linearizing their dynamic model, but the decoupling matrix had to be full rank, meaning that the initial state of the system had to be specified. Galicki [33] addressed the position control problem for mobile manipulators operating with state constraints in a task space, however, no experimental verification was provided. Peng *et al.* [8] proposed an adaptive sliding mode tracking controller to deal with the unknown upper bounds of a mobile manipulator's parameter uncertainties and external disturbances to achieve accurate position tracking. Yet, the complicated system dynamics are difficult to be handled in practical application. Sliding mode control [34] and adaptive control [35] have also been proposed to achieve finite-time convergence for robotic systems with unknown dynamics and disturbances, with their performance validated through simulation results. However, the tracking accuracy remains a challenge due to the complexity of the system dynamics [36].

The above-mentioned control approaches have led to the employment of nonlinear model-based or model-free techniques, where a well-designed feedforward control term (derived by dynamic model or data-driven model) can partially address the system's nonlinearities. However, the exact feedforward control term of a WMM system is hard or even impossible to derive due to the severe joint coupling, nonlinear friction, wheel-ground interaction, etc. [37]. In order to cope with this challenge, Zhu [38] proposed an adaptive nonlinear model-based control approach called virtual decomposition control (VDC) to model and control multi-DoF robotic systems inspired by the Newton–Euler formulation. The primary concept of this approach is to virtually decompose the entire robotic system into several independent subsystems. Each subsystem is connected with the contiguous subsystem through the "force" element composed of force/torque (F/T) and the "velocity" element comprised of linear velocity and angular velocity. The dynamic interaction between the adjacent subsystems is described using the unique feature of VDC called virtual power flow (VPF). Compared with the dynamic model based on the Lagrangian formulation, this method's computation is proportional to the number of the subsystems (the calculation of the Lagrangian high-order dynamic model is proportional to the fourth power of the system's DoF [38]). Therefore, the computational efficiency improves significantly.

The VDC has demonstrated remarkable performance in handling complex robotic systems, including electrically driven manipulators [25], [39], mobile manipulators [40], and exoskeleton robots [41]. Based on VDC, Xia *et al.* [42] developed a dynamic model of a 6-DoF manipulator considering joint elasticity and friction. Despite the effectiveness of their modeling approach being experimentally verified, they failed to provide a control method to match. Koivumäki and Mattila [43] developed an impedance control method for multi-DoF hydraulic manipulators with highly nonlinear dynamics, which guaranteed the L_2 and L_∞ stability of the system in both free space and contact environments. The joint friction term, however, was not considered. The VDC method was adopted by Brahmi *et al.* [44] in order to overcome the parameter coupling of nonholonomic wheeled mobile manipulators (NWMMs). This increases the flexibility of the control system when the configuration of the NWMMs changes. Despite this, no wheel-ground interaction was considered. Jafarinasab *et al.* [40] developed a model-based adaptive motion control algorithm followed the VDC method for an underactuated aerial robotic manipulator, but joint dynamics were not taken into account. Sun *et al.* [45] presented a high-performance controller with L_2 and L_∞ stability to realize the precise position trajectory tracking control for exoskeleton robots, while joint flexibility was not considered.

The dynamic control of complex robotic systems presents significant challenges, particularly as the number of DoF increases, leading to a substantial computational burden that complicates real-time implementation [43], [46]. Furthermore, the control of WMMs is further complicated by factors such as unknown dynamic parameters, nonlinear friction effects, structural elasticity, and wheel-ground interactions [47]. While adaptive control approaches, including model-based feedback and model-free methods, have been widely explored for applications involving robot disturbances, existing studies have not yet addressed the complete-dynamics-based control of a multi-DoF WMM coupled with a collaborative manipulator. Notably, experimental implementation and rigorous stability validation of such a control framework remain unexplored in the current literature.

To address the limitations in existing research, this paper proposes a VDC-based trajectory tracking control approach for WMMs with flexible joints. The main contributions are as follows: 1) A stability-guaranteed trajectory tracking control method is proposed based on the full nonlinear dynamics of the WMM; 2) The control framework explicitly considers joint flexibility and wheel-ground interactions to improve model accuracy; 3) A rigorous stability analysis is conducted, demonstrating the asymptotic convergence of trajectory tracking errors for the closed-loop system; 4) The proposed control approach is experimentally validated on a physical WMM system comprising an omnidirectional platform and a 7-DoF serial manipulator, showcasing its practical effectiveness. These contributions address the absence of experimentally validated, full-dynamics-based control frameworks in the current literature.

The remainder of this paper is organized as follows. Section II presents the kinematic and dynamic models of a WMM based on VDC. The proposed task-space trajectory tracking method via VDC is described in Section III. Section IV provides the stability proof of the approach. Experiments that demonstrate the validity and performance of the proposed method are presented in Section V. Section VI concludes the manuscript.

II. VDC-based Kinematics and Dynamics of Wheeled Mobile Manipulators

In this section, the virtual decomposition schematic, kinematic model, and dynamic model of WMMs integrated with a MP and a multi-DoF manipulator are provided. Section II-A presents the virtual decomposition schematic of the WMMs, Section II-B presents their kinematic model, and their dynamic model is shown in Section II-C.

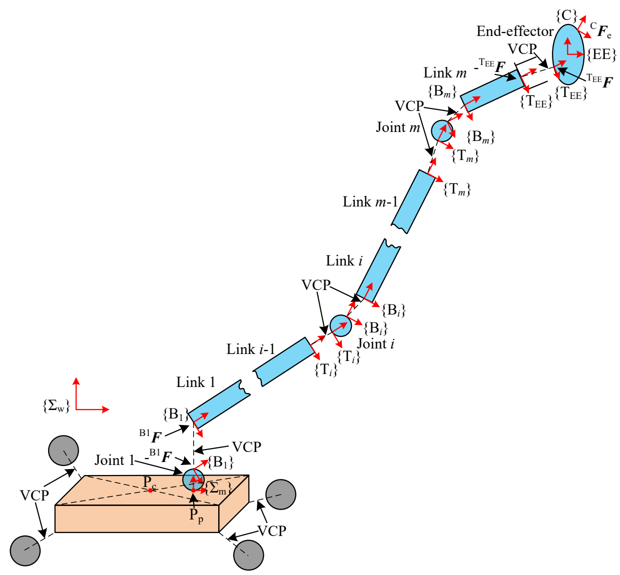

Figure 1: Virtual decomposition schematic of an omnidirectional WMM.

A. Virtual Decomposition Schematic of Wheeled Mobile Manipulators

First, the concept of virtual cutting point (VCP) will be presented, which is of great importance to the VDC approach because it can conceptually decompose a complex robotic system into several subsystems, which is defined in Definition 1.

Definition 1. *A cutting point is a directed separation interface that conceptually cuts through a rigid body. The two parts caused by the virtual cut share equal pose. The cutting point is expressed as a driving cutting point by one part and is simultaneously expressed as a driven cutting point by the other part. The force/moment vector is exerted from which the cutting point is expressed as a driving cutting point to which the cutting point is expressed as a driven cutting point.*

Fig. 1 presents the virtual decomposition schematic of an omnidirectional WMM. The WMM consists of a four-wheel MP and an m-DoF robotic manipulator. Point $P_{\rm p}$ is the connection point between the MP and the manipulator. The manipulator system is virtually decomposed into $2m+1$ subsystems, including n joints, n links, and one EE. As shown in Fig. 1, we denote $\{\Sigma_{\rm m}\}$ as the manipulator reference frame. $2m$ virtual cutting points (VCPs) $(\mathrm{B}_1, \cdots, \mathrm{B}_m, \mathrm{T}_2, \cdots, \mathrm{T}_m, \mathrm{T}_{\rm EE})$ have been defined (the definition of VCP is shown below). Frame $\{\mathrm{T}_{\rm EE}\}$ is located at the connection point between the $m^{\rm th}$ link and the EE. Also, frame $\{\mathrm{C}\}$ is located at the point where the contact occurs. It should be emphasized that the EE has only one VCP.

As for the MP in Fig. 1, its detailed virtual decomposition schematic is shown in Fig. 2. By adding a massless virtual 6-DoF manipulator between the MP body and the ground, the MP can be regarded as an open-chain system. Then, ten VCPs are fixed between the system, and the MP is virtually decomposed into ten subsystems: one MP body, four wheels, four wheel joints, and one massless 6-DoF manipulator. Here, frame $\{\mathrm{P_p}\}$ is attached onto the VCP between the MP and the manipulator (its z-axis is parallel to the rotation axis of the manipulator's first joint); frame $\{\mathrm{P_c}\}$ is attached onto the central point of the MP (this point is also the location of the VCP between the MP and the virtual manipulator); frames $\{\mathrm{A_{fl}}\}$, $\{\mathrm{A_{fr}}\}$, $\{\mathrm{A_{bl}}\}$, and $\{\mathrm{A_{br}}\}$ are attached onto the VCP between the MP body and the four wheels, respectively. Four auxiliary VCPs are set on each of the four wheels to decompose the wheels and their joints, and then four frames $\{\mathrm{W_{fl}}\}$, $\{\mathrm{W_{fr}}\}$, $\{\mathrm{W_{bl}}\}$, and $\{\mathrm{W_{br}}\}$ are attached onto the four auxiliary VCPs. It is worth mentioning that the z-axes of the above eight frames are parallel to their respective wheel joint rotation axes. Besides, four frames $\{\mathrm{C_{fl}}\}$, $\{\mathrm{C_{fr}}\}$, $\{\mathrm{C_{bl}}\}$, and $\{\mathrm{C_{br}}\}$ are attached respectively onto the contact points between the four wheels and the ground to describe their interaction forces.

In summary, combined with Definition 1, the VCPs contained in each MP subsystem can be concluded as follows:

- The left front wheel has only one driven cutting point associated with frame $\{\mathrm{W_{fl}}\}$.
- The right front wheel has only one driven cutting point associated with frame $\{\mathrm{W_{fr}}\}$.
- The left rear wheel has only one driven cutting point associated with frame $\{\mathrm{W_{bl}}\}$.
- The right rear wheel has only one driven cutting point associated with frame $\{\mathrm{W_{br}}\}$.
- The left front wheel joint has one driving cutting point associated with frame $\{\mathrm{W_{fl}}\}$ and one driven cutting point associated with frame $\{\mathrm{A_{fl}}\}$.
- The right front wheel joint has one driving cutting point associated with frame $\{\mathrm{W_{fr}}\}$ and one driven cutting point associated with frame $\{\mathrm{A_{fr}}\}$.
- The left rear wheel joint has one driving cutting point associated with frame $\{\mathrm{W_{bl}}\}$ and one driven cutting point associated with frame $\{\mathrm{A_{bl}}\}$.
- The right rear wheel joint has one driving cutting point associated with frame $\{\mathrm{W_{br}}\}$ and one driven cutting point associated with frame $\{\mathrm{A_{br}}\}$.
- The MP body has five driving cutting points associated with frame $\{\mathrm{P_p}\}$, $\{\mathrm{A_{fl}}\}$, $\{\mathrm{A_{fr}}\}$, $\{\mathrm{A_{bl}}\}$, and $\{\mathrm{A_{br}}\}$, respectively, and one driven cutting point associated with frame $\{\mathrm{P_c}\}$.
- The massless virtual manipulator has only one driving cutting point associated with frame $\{\mathrm{P_c}\}$.

When the manipulator is mounted on the MP, the manipulator will have one more VCP to decompose the manipulator and the MP, that is, the first joint of the manipulator will have another driven cutting point associated with frame $\{\mathrm{P_p}\}$.

B. Kinematic Modeling of Wheeled Mobile Manipulators

In line with the virtual decomposition model of the WMM described in Section II-A, the kinematics of the WMM can be derived. We will first present the kinematic model of the MP. It is assumed that a pure rolling contact exists between the mobile base's wheels and the ground (i.e., no slippage). With this assumption, the kinematics of the MP can be derived as

$$\dot{\boldsymbol{q}}_{\mathrm{p}} = \boldsymbol{\Psi}(\boldsymbol{q}_{\mathrm{p}})\boldsymbol{v}_{\mathrm{p}}, \tag{1}$$

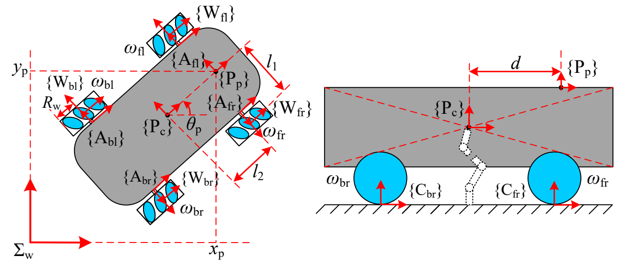

Figure 2: Virtual decomposition schematic of an MP.

where $\dot{\boldsymbol{q}}_{\mathrm{p}} \in \mathbb{R}^{n_{\mathrm{p}}}$ is the generalized coordinate vector of the MP with n_{p} denoting its dimension, $\boldsymbol{v}_{\mathrm{p}} \in \mathbb{R}^{p}$ is the velocity vector of the wheels with p denoting its dimension, and $\boldsymbol{\Psi}(\boldsymbol{q}_{\mathrm{p}}) \in \mathbb{R}^{n_{\mathrm{p}} \times p}$ is the constraint matrix of the MP.

According to Figs. 1 and 2, $\{\Sigma_{\mathrm{w}}\}$ denotes the world frame, R_{w} denotes the wheel radius, l_1 and l_2 denote the distance between the wheel axis and point $\mathrm{P_c}$, d denotes the horizontal distance between points $\mathrm{P_b}$ and $\mathrm{P_c}$. Here, in Fig. 2, the generalized coordinate vector of the MP is defined as $\boldsymbol{q}_{\mathrm{p}} = [x_{\mathrm{p}}, y_{\mathrm{p}}, \theta_{\mathrm{p}}]^{\mathrm{T}} \in \mathbb{R}^3$. Also, the velocity command of the wheels is defined as $\boldsymbol{v}_{\mathrm{p}} = [\omega_{\mathrm{fl}}, \omega_{\mathrm{fr}}, \omega_{\mathrm{bl}}, \omega_{\mathrm{br}}]^{\mathrm{T}} \in \mathbb{R}^4$. According to the structure of the MP and (1), the constraint matrix $\boldsymbol{\Psi}(\boldsymbol{q}_{\mathrm{p}})$, which transfers the wheel velocities to the MP's generalized velocities, can be expressed as

$$\boldsymbol{\Psi}(\boldsymbol{q}_{\mathrm{p}}) = \boldsymbol{J}_{\mathrm{x}}(\boldsymbol{q}_{\mathrm{p}})(\boldsymbol{J}_{\mathrm{y}} + \boldsymbol{J}_{\mathrm{z}}) \tag{2}$$

with $\boldsymbol{J}_{\mathrm{x}} = \begin{bmatrix} \cos\theta_{\mathrm{p}} & -\sin\theta_{\mathrm{p}} & 0 \\ \sin\theta_{\mathrm{p}} & \cos\theta_{\mathrm{p}} & 0 \\ 0 & 0 & 1 \end{bmatrix}$, $\boldsymbol{J}_{\mathrm{y}} = \frac{R_{\mathrm{w}}}{4}\begin{bmatrix} 1 & 1 & 1 & 1 \\ -1 & 1 & 1 & -1 \\ \frac{-1}{l_1+l_2} & \frac{1}{l_1+l_2} & \frac{-1}{l_1+l_2} & \frac{1}{l_1+l_2} \end{bmatrix}$, and $\boldsymbol{J}_{\mathrm{z}} = \frac{R_{\mathrm{w}}d}{4}\begin{bmatrix} 0 & 0 & 0 & 0 \\ \frac{-1}{l_1+l_2} & \frac{1}{l_1+l_2} & \frac{-1}{l_1+l_2} & \frac{1}{l_1+l_2} \\ 0 & 0 & 0 & 0 \end{bmatrix}$.

Then, the kinematic model of the manipulator will be established followed by the introduction of the term of linear/angular velocity and force/torque transformations. Consider $\{\mathrm{A}\}$ as a frame attached to a rigid body. Let ${}^{\mathrm{A}}\boldsymbol{v} \in \mathbb{R}^3$ and ${}^{\mathrm{A}}\boldsymbol{\omega} \in \mathbb{R}^3$ be the linear and angular velocity vectors of frame $\{\mathrm{A}\}$, and the linear/angular velocity vector of frame $\{\mathrm{A}\}$ is written as ${}^{\mathrm{A}}\boldsymbol{V} = \left[{}^{\mathrm{A}}\boldsymbol{v}^{\mathrm{T}},\ {}^{\mathrm{A}}\boldsymbol{\omega}^{\mathrm{T}}\right]^{\mathrm{T}}$. Similarly, let ${}^{\mathrm{A}}\boldsymbol{f} \in \mathbb{R}^3$ and ${}^{\mathrm{A}}\boldsymbol{m} \in \mathbb{R}^3$ be the force and torque vectors of frame $\{\mathrm{A}\}$, and the F/T vector of frame $\{\mathrm{A}\}$ is written as ${}^{\mathrm{A}}\boldsymbol{F} = \left[{}^{\mathrm{A}}\boldsymbol{f}^{\mathrm{T}},\ {}^{\mathrm{A}}\boldsymbol{m}^{\mathrm{T}}\right]^{\mathrm{T}}$. Then, consider two frames, expressed as $\{\mathrm{A}\}$ and $\{\mathrm{B}\}$, being fixed to a rigid body, no matter whether it is moving or subject to physical force and torque vectors. The following relations hold

$${}^{\mathrm{B}}\boldsymbol{V} = {}^{\mathrm{A}}\boldsymbol{U}_{\mathrm{B}}^{\mathrm{T}}\,{}^{\mathrm{A}}\boldsymbol{V}, \quad {}^{\mathrm{A}}\boldsymbol{F} = {}^{\mathrm{A}}\boldsymbol{U}_{\mathrm{B}}\,{}^{\mathrm{B}}\boldsymbol{F}, \tag{3}$$

where ${}^{\mathrm{A}}\boldsymbol{U}_{\mathrm{B}} \in \mathbb{R}^{6\times 6}$ is an F/T transformation matrix that transforms the F/T vector expressed in frame $\{\mathrm{B}\}$ to the same F/T vector expressed in frame $\{\mathrm{A}\}$.

Thus, the linear/angular velocity vector of each manipulator's subsystem in its corresponding frame can be expressed as

$$^{\mathrm{B}_1}\boldsymbol{V} = \boldsymbol{z}\dot{q}_{\mathrm{m},1}, \tag{4a}$$
$$^{\mathrm{T}_i}\boldsymbol{V} = {}^{\mathrm{B}_{i-1}}\boldsymbol{U}_{\mathrm{T}_i}^{\mathrm{T}}\,{}^{\mathrm{B}_{i-1}}\boldsymbol{V}, \tag{4b}$$
$$^{\mathrm{B}_i}\boldsymbol{V} = \boldsymbol{z}\dot{q}_{\mathrm{m},i} + {}^{\mathrm{T}_i}\boldsymbol{U}_{\mathrm{B}_i}^{\mathrm{T}}\,{}^{\mathrm{T}_i}\boldsymbol{V} = \boldsymbol{z}\dot{q}_{\mathrm{m},i} + {}^{\mathrm{B}_{i-1}}\boldsymbol{U}_{\mathrm{B}_i}^{\mathrm{T}}\,{}^{\mathrm{B}_{i-1}}\boldsymbol{V}, \tag{4c}$$
$$^{\mathrm{T}_{\mathrm{EE}}}\boldsymbol{V} = {}^{\mathrm{B}_n}\boldsymbol{U}_{\mathrm{T}_{\mathrm{EE}}}^{\mathrm{T}}\,{}^{\mathrm{B}_n}\boldsymbol{V}, \tag{4d}$$
$$^{\mathrm{EE}}\boldsymbol{V} = {}^{\mathrm{T}_{\mathrm{EE}}}\boldsymbol{U}_{\mathrm{EE}}^{\mathrm{T}}\,{}^{\mathrm{T}_{\mathrm{EE}}}\boldsymbol{V}, \tag{4e}$$
$$^{\mathrm{C}}\boldsymbol{V}_{\mathrm{e}} = {}^{\mathrm{EE}}\boldsymbol{U}_{\mathrm{C}}^{\mathrm{T}}\,{}^{\mathrm{EE}}\boldsymbol{V}, \tag{4f}$$

where $i = 2, 3, \ldots, m$, $\boldsymbol{z} = [0, 0, 0, 0, 0, 1]^{\mathrm{T}} \in \mathbb{R}^6$, $\dot{q}_{m,i}$ represents the angular velocity of the i^{th} joint, and ${}^{\mathrm{T}}\boldsymbol{U}_{\mathrm{B}}$ denotes the force/moment transformation matrix from $\{\mathrm{B}\}$ to $\{\mathrm{T}\}$ with its definition in (3).

According to (4), the transformation matrix between ${}^{\mathrm{C}}\boldsymbol{V}_{\mathrm{e}} \in \mathbb{R}^6$ and the generalized joint velocity vector $\dot{\boldsymbol{q}}_{\mathrm{m}} = [\dot{q}_{\mathrm{m},1}, \dot{q}_{\mathrm{m},2}, \ldots, \dot{q}_{\mathrm{m},m}]^{\mathrm{T}} \in \mathbb{R}^m$, also called the manipulator Jacobian matrix $\boldsymbol{J}_{\mathrm{me}} \in \mathbb{R}^{6\times m}$, can be expressed as

$$^{\mathrm{C}}\boldsymbol{V}_{\mathrm{e}} = \boldsymbol{J}_{\mathrm{me}}\dot{\boldsymbol{q}}_{\mathrm{m}} = \left[{}^{\mathrm{B}_1}\boldsymbol{U}_{\mathrm{C}}^{\mathrm{T}}\boldsymbol{z}, {}^{\mathrm{B}_2}\boldsymbol{U}_{\mathrm{C}}^{\mathrm{T}}\boldsymbol{z}, \ldots, {}^{\mathrm{B}_m}\boldsymbol{U}_{\mathrm{C}}^{\mathrm{T}}\boldsymbol{z}\right]\dot{\boldsymbol{q}}_{\mathrm{m}}. \tag{5}$$

As shown in Fig. 1, we fix the manipulator reference frame $\{\Sigma_{\mathrm{m}}\}$ with point P_{p} to set up a WMM, and make sure that the x-axis of frame $\{\Sigma_{\mathrm{m}}\}$ coincides with the MP's heading direction. It should be noted that the reference frame of Jacobian matrix $\boldsymbol{J}_{\mathrm{me}}$ is frame $\{\mathrm{C}\}$, if we want to replace it with the world frame $\{\Sigma_{\mathrm{w}}\}$, then, the new Jacobian matrix can be derived as

$$\boldsymbol{J}_{\mathrm{m}} = \begin{bmatrix} {}^{\Sigma_{\mathrm{w}}}\boldsymbol{R}_{\mathrm{C}} & \boldsymbol{0}_{3\times 3} \\ \boldsymbol{0}_{3\times 3} & {}^{\Sigma_{\mathrm{w}}}\boldsymbol{R}_{\mathrm{C}} \end{bmatrix}\boldsymbol{J}_{\mathrm{me}}, \tag{6}$$

where $\boldsymbol{J}_{\mathrm{m}} \in \mathbb{R}^{6\times m}$ represents the manipulator's Jacobian matrix in $\{\Sigma_{\mathrm{w}}\}$, and ${}^{\Sigma_{\mathrm{w}}}\boldsymbol{R}_{\mathrm{C}} \in \mathbb{R}^{3\times 3}$ represents the rotation matrix from $\{\mathrm{C}\}$ to $\{\Sigma_{\mathrm{w}}\}$.

The generalized velocity vector of the manipulator is selected as its joint velocity vector, which is $\dot{\boldsymbol{q}}_{\mathrm{m}} = \boldsymbol{v}_{\mathrm{m}}$, where $\boldsymbol{v}_{\mathrm{m}} \in \mathbb{R}^m$ denotes the manipulator's joint velocity vector. Let us define the configuration vector of the WMM as $\boldsymbol{q} = \left[\boldsymbol{q}_{\mathrm{p}}^{\mathrm{T}},\ \boldsymbol{q}_{\mathrm{m}}^{\mathrm{T}}\right]^{\mathrm{T}} \in \mathbb{R}^n$, and its velocity input vector as $\boldsymbol{v} = \left[\boldsymbol{v}_{\mathrm{p}}^{\mathrm{T}},\ \boldsymbol{v}_{\mathrm{m}}^{\mathrm{T}}\right]^{\mathrm{T}} \in \mathbb{R}^{\bar{n}}$, where $n = n_{\mathrm{p}} + m$, $\bar{n} = p + m$. The pose of the EE in $\{\Sigma_{\mathrm{w}}\}$ is defined as $\boldsymbol{x}_{\mathrm{e}} \in \mathbb{R}^r$ with r representing its dimension; then, the forward kinematics at velocity level of the entire WMM can be expressed as

$$\begin{aligned} \dot{\boldsymbol{x}}_{\mathrm{e}} &= \left[\boldsymbol{J}_{\mathrm{p}}(\boldsymbol{q}), \boldsymbol{J}_{\mathrm{m}}(\boldsymbol{q})\right]\begin{bmatrix}\dot{\boldsymbol{q}}_{\mathrm{p}} \\ \dot{\boldsymbol{q}}_{\mathrm{m}}\end{bmatrix} = \left[\boldsymbol{J}_{\mathrm{p}}(\boldsymbol{q}), \boldsymbol{J}_{\mathrm{m}}(\boldsymbol{q})\right]\begin{bmatrix}\boldsymbol{\Psi}(\boldsymbol{q}_{\mathrm{p}})\boldsymbol{v}_{\mathrm{p}} \\ \boldsymbol{v}_{\mathrm{m}}\end{bmatrix} \\ &= \left[\boldsymbol{J}_{\mathrm{p}}(\boldsymbol{q})\boldsymbol{\Psi}(\boldsymbol{q}_{\mathrm{p}}), \boldsymbol{J}_{\mathrm{m}}(\boldsymbol{q})\right]\begin{bmatrix}\boldsymbol{v}_{\mathrm{p}} \\ \boldsymbol{v}_{\mathrm{m}}\end{bmatrix} = \boldsymbol{J}(\boldsymbol{q})\boldsymbol{v}, \end{aligned} \tag{7}$$

where $\boldsymbol{J}_{\mathrm{p}} \in \mathbb{R}^{r\times n_{\mathrm{p}}}$ and $\boldsymbol{J} \in \mathbb{R}^{r\times\bar{n}}$ denotes the Jacobian matrices of the MP and WMM in $\{\Sigma_{\mathrm{w}}\}$, respectively.

C. Dynamic Modeling of Wheeled Mobile Manipulators

Consider a rigid object with frame $\{\mathrm{A}\}$ fixed; then, the general formulation of its dynamics, in which frame $\{\mathrm{A}\}$ is used as the reference frame, can be expressed as [38]

$$\boldsymbol{M}_{\mathrm{A}}\frac{\mathrm{d}}{\mathrm{d}t}({}^{\mathrm{A}}\boldsymbol{V}) + \boldsymbol{C}_{\mathrm{A}}({}^{\mathrm{A}}\boldsymbol{\omega}){}^{\mathrm{A}}\boldsymbol{V} + \boldsymbol{G}_{\mathrm{A}} = {}^{\mathrm{A}}\boldsymbol{F}^{*}, \tag{8}$$

where $\boldsymbol{M}_{\mathrm{A}} \in \mathbb{R}^{6\times 6}$ is the mass matrix, $\boldsymbol{C}_{\mathrm{A}}({}^{\mathrm{A}}\boldsymbol{\omega}) \in \mathbb{R}^{6\times 6}$ is the matrix of Coriolis and centrifugal terms, $\boldsymbol{G}_{\mathrm{A}} \in \mathbb{R}^6$ is the gravity term, and ${}^{\mathrm{A}}\boldsymbol{F}^{*} \in \mathbb{R}^6$ is the net F/T vector of the rigid body expressed in frame $\{\mathrm{A}\}$. The aforementioned inertia and similar parameters are classified as internal and parametric uncertainties. In the following sections, these parameters will be estimated using adaptive control with predefined upper and lower bounds.

According to Fig. 1 and (8), the force resultant equations of the m links and the EE on the manipulator can be calculated as

$$^{\mathrm{EE}}\boldsymbol{F}^{*} = {}^{\mathrm{EE}}\boldsymbol{U}_{\mathrm{T}_{\mathrm{EE}}}\,{}^{\mathrm{T}_{\mathrm{EE}}}\boldsymbol{F} - {}^{\mathrm{EE}}\boldsymbol{U}_{\mathrm{C}}\,{}^{\mathrm{C}}\boldsymbol{F}_{\mathrm{e}}, \tag{9a}$$
$$^{\mathrm{B}_m}\boldsymbol{F}^{*} = {}^{\mathrm{B}_m}\boldsymbol{F} - {}^{\mathrm{B}_m}\boldsymbol{U}_{\mathrm{T}_{\mathrm{EE}}}\,{}^{\mathrm{T}_{\mathrm{EE}}}\boldsymbol{F}, \tag{9b}$$
$$^{\mathrm{T}_i}\boldsymbol{F} = {}^{\mathrm{T}_i}\boldsymbol{U}_{\mathrm{B}_i}\,{}^{\mathrm{B}_i}\boldsymbol{F}, \quad i = m, \ldots, 2, \tag{9c}$$
$$^{\mathrm{B}_i}\boldsymbol{F}^{*} = {}^{\mathrm{B}_i}\boldsymbol{F} - {}^{\mathrm{B}_i}\boldsymbol{U}_{\mathrm{T}_{i+1}}\,{}^{\mathrm{T}_{i+1}}\boldsymbol{F}, \quad i = m-1, \ldots, 1, \tag{9d}$$

where ${}^{(\cdot)}\boldsymbol{F}^{*} \in \mathbb{R}^6$ is the net F/T vector at frame $\{(\cdot)\}$, ${}^{\mathrm{C}}\boldsymbol{F}_{\mathrm{e}} \in \mathbb{R}^6$ is the external F/T vector exerted at the contact frame $\{\mathrm{C}\}$, and ${}^{\mathrm{A}}\boldsymbol{F} \in \mathbb{R}^6$, $\mathrm{A} \in \{\mathrm{T}_{\mathrm{EE}}, \mathrm{B}_i, \mathrm{T}_i\}$, denotes the driving F/T vector of each link at its corresponding frame. The external force/torque vector ${}^{\mathrm{C}}\boldsymbol{F}_{\mathrm{e}}$ is categorized as an external and nonparametric uncertainty. In the following sections, it will be computed using a linearized equation model. The purpose of (9) is to calculate the driving F/T vector from each joint to the next link, ${}^{\mathrm{B}_i}\boldsymbol{F}$, according to (8), via an iterative approach.

The dynamics of the manipulator joints are also considered to improve the modeling accuracy. For most collaborative manipulators, their joints are usually mixed with transmission elasticity, motor inertia, and friction [48], when taking the friction term on both the motor and link sides and the joint elasticity into account, the dynamic model of i^{th} $(i = 1, 2, \ldots, m)$ joint can be presented as [49]

$$\tau_{\mathrm{fq},i}(\dot{q}_{\mathrm{m},i}) = \tau_{\mathrm{t},i} - \tau_{\mathrm{a},i}, \tag{10a}$$
$$\tau_{\mathrm{t},i} = k_{\mathrm{f},i}(\phi_{\mathrm{m},i} - q_{\mathrm{m},i}), \tag{10b}$$
$$\mathcal{I}_{\mathrm{m},i}\ddot{\phi}_{\mathrm{m},i} + \tau_{\mathrm{f}\phi,i}(\dot{\phi}_{\mathrm{m},i}) = \tau_i - \tau_{\mathrm{t},i}, \tag{10c}$$
$$\tau_{\mathrm{fq},i}(\dot{q}_{\mathrm{m},i}) = f_{\mathrm{vq},i}\dot{q}_{\mathrm{m},i} + f_{\mathrm{cq},i}\mathrm{sign}(\dot{q}_{\mathrm{m},i}), \tag{10d}$$
$$\tau_{\mathrm{f}\phi,i}(\dot{\phi}_{\mathrm{m},i}) = f_{\mathrm{v}\phi,i}\dot{\phi}_{\mathrm{m},i} + f_{\mathrm{c}\phi,i}\mathrm{sign}(\dot{\phi}_{\mathrm{m},i}), \tag{10e}$$

where $\tau_{\mathrm{fq},i}$ is the link-side friction torque; $\tau_{\mathrm{t},i}$ is the effective transmission input torque; $\tau_{\mathrm{a},i}$ is the torque output of the joint toward the corresponding link, which is $\tau_{\mathrm{a},i} = \boldsymbol{z}^{\mathrm{T}}\,{}^{\mathrm{B}_i}\boldsymbol{F}$; $k_{\mathrm{f},i}$ is the joint stiffness coefficient; $\phi_{\mathrm{m},i}$ is the motor-side joint position; $\mathcal{I}_{\mathrm{m},i}$ is the joint moment of inertia; $\tau_{\mathrm{f}\phi,i}$ is the motor-side friction torque; τ_i is the motor control torque; $f_{\mathrm{vq},i}$ and $f_{\mathrm{cq},i}$ denote the link-side viscous and Coulomb friction coefficients; $f_{\mathrm{v}\phi,i}$ and $f_{\mathrm{c}\phi,i}$ represent the motor-side viscous and Coulomb friction coefficients; and $\mathrm{sign}(\dot{q})$ is defined as $\mathrm{sign}(\dot{q}) = \begin{cases} \dot{q}/|\dot{q}|, & \dot{q} \neq 0 \\ 0, & \dot{q} = 0 \end{cases}$. Here, joint flexibility and nonlinear friction effects are categorized as internal and nonparametric uncertainties. However, suitable linearized models can be established to describe them.

According to Fig. 1 and (9), the supporting force from the MP to the manipulator can be exerted through the connection point $\mathrm{P_p}$, which is expressed as

$$ {}^{\mathrm{P_p}}\boldsymbol{F} = {}^{\mathrm{P_p}}\boldsymbol{U}_{\mathrm{B_1}}\, {}^{\mathrm{B_1}}\boldsymbol{F}, \tag{11} $$

where ${}^{\mathrm{P_p}}\boldsymbol{F} \in \mathbb{R}^6$ denotes the F/T vector from the MP to the manipulator expressed in frame $\{\mathrm{P_p}\}$ and ${}^{\mathrm{P_p}}\boldsymbol{U}_{\mathrm{B_1}} \in \mathbb{R}^{6\times 6}$ is the F/T transformation matrix from frame $\{\mathrm{B_1}\}$ to frame $\{\mathrm{P_p}\}$. Thus, combined with (11), the force applied from the manipulator to the MP can be presented as $-{}^{\mathrm{P_p}}\boldsymbol{F}$.

Then, the dynamic model of the MP will be presented. In line with (2), the generalized velocity vector of the wheels is written as

$$ {}^{\mathrm{W}_i}\boldsymbol{V} = \boldsymbol{z}_{\mathrm{w}}\omega_i + {}^{\mathrm{A}_i}\boldsymbol{U}_{\mathrm{W}_i}^{\mathrm{T}}\, {}^{\mathrm{A}_i}\boldsymbol{V}, \tag{12} $$

where $i \in \{\mathrm{fl}, \mathrm{fr}, \mathrm{bl}, \mathrm{br}\}$ denotes the wheel ID, ω_i denotes the angular velocity of the wheel joint with ID i, and $\boldsymbol{z}_{\mathrm{w}} \in \mathbb{R}^6$ is a constant vector, $\boldsymbol{z}_{\mathrm{w}} = [0, 0, 0, 0, 0, 1]^{\mathrm{T}}$. Define $0 \leqslant n_{\mathrm{wg},i} < 6$ as the constraint number of wheel-ground contact, the velocity of each wheel-ground contact point in contact frame $\{\mathrm{C}_i\}$ can be expressed as

$$ {}^{\mathrm{C}_i}\boldsymbol{V}_{\mathrm{wg}} = {}^{\mathrm{W}_i}\boldsymbol{U}_{\mathrm{C}_i}^{\mathrm{T}}\, {}^{\mathrm{W}_i}\boldsymbol{V} = \boldsymbol{T}_{\mathrm{c},i}\boldsymbol{\chi}_i, \tag{13} $$

where $\boldsymbol{T}_{\mathrm{c},i} \in \mathbb{R}^{6\times(6-n_{\mathrm{wg},i})}$ denotes a matrix of full column-rank with each column containing a single *one* and five *zeros* and $\boldsymbol{\chi}_i \in \mathbb{R}^{6-n_{\mathrm{wg},i}}$ is an independent velocity coordinate vector of frame $\{\mathrm{C}_i\}$.

Similar to (9), the force resultant equations of the wheels can be expressed as

$$ {}^{\mathrm{W}_i}\boldsymbol{F}^{*} = {}^{\mathrm{W}_i}\boldsymbol{F} - {}^{\mathrm{W}_i}\boldsymbol{U}_{\mathrm{C}_i}\, {}^{\mathrm{C}_i}\boldsymbol{F}_{\mathrm{wg}}, \tag{14a} $$
$$ {}^{\mathrm{W}_i}\boldsymbol{F} = {}^{\mathrm{W}_i}\boldsymbol{U}_{\mathrm{A}_i}\, {}^{\mathrm{A}_i}\boldsymbol{F}, \tag{14b} $$

where ${}^{\mathrm{W}_i}\boldsymbol{F} \in \mathbb{R}^6$ and ${}^{\mathrm{A}_i}\boldsymbol{F} \in \mathbb{R}^6$ are the F/T vector from the wheel joint to the wheel and from the MP body to the wheel joint expressed in their respective frames, and ${}^{\mathrm{C}_i}\boldsymbol{F}_{\mathrm{wg}} \in \mathbb{R}^6$ denotes the wheel-ground contact force vector expressed in frame $\{\mathrm{C}_i\}$. Wheel-ground contact is typically unknown and categorized as an external and stochastic uncertainty. In the following, it is represented as a combination of components in the motion and constraint configuration spaces.

Here, ${}^{\mathrm{C}_i}\boldsymbol{F}_{\mathrm{wg}} \in \mathbb{R}^6$ in (14a) can be further expressed as

$$ {}^{\mathrm{C}_i}\boldsymbol{F}_{\mathrm{wg}} = \boldsymbol{T}_{\mathrm{c},i}\boldsymbol{\psi}_i + \boldsymbol{T}_{\mathrm{f},i}\boldsymbol{\varphi}_i, \tag{15} $$

where $\boldsymbol{T}_{\mathrm{f},i} \in \mathbb{R}^{6\times n_{\mathrm{wg},i}}$ denotes a matrix of full column-rank with each column containing a single *one* and five *zeros*, $\boldsymbol{\psi}_i \in \mathbb{R}^{6-n_{\mathrm{wg},i}}$ and $\boldsymbol{\varphi}_i \in \mathbb{R}^{n_{\mathrm{wg},i}}$ represent two coordinate vectors in the motion and constraint configuration spaces, respectively. The selection of $\boldsymbol{T}_{\mathrm{c},i} \in \mathbb{R}^{6\times(6-n_{\mathrm{wg},i})}$ and $\boldsymbol{T}_{\mathrm{f},i} \in \mathbb{R}^{6\times n_{\mathrm{wg},i}}$ ensures that $\boldsymbol{T}_{\mathrm{c},i}^{\mathrm{T}}\,\boldsymbol{T}_{\mathrm{c},i} = \boldsymbol{I}_{6-n_{\mathrm{wg},i}}$, $\boldsymbol{T}_{\mathrm{f},i}^{\mathrm{T}}\,\boldsymbol{T}_{\mathrm{f},i} = \boldsymbol{I}_{n_{\mathrm{wg},i}}$, and $\boldsymbol{T}_{\mathrm{c},i}^{\mathrm{T}}\,\boldsymbol{T}_{\mathrm{f},i} = \boldsymbol{0}$ hold.

In free-motion space, the independent force coordinate vector $\boldsymbol{\psi}_i \in \mathbb{R}^{6-n_{\mathrm{wg},i}}$ in (15) can also be linearly parameterized as

$$ \boldsymbol{\psi}_i = \boldsymbol{Y}_{\mathrm{c},i}\boldsymbol{\theta}_{\mathrm{c},i}, \tag{16} $$

where $\boldsymbol{Y}_{\mathrm{c},i}$ is a regression matrix and $\boldsymbol{\theta}_{\mathrm{c},i}$ denotes the unknown parameter vector.

Unlike the flexible manipulator joint model expressed in (10), it is assumed that the wheel joints are rigid, and their dynamic models can be simplified as [38]

$$ \mathcal{I}_i\dot{\omega}_i + f_{\mathrm{v},i}\omega_i + f_{\mathrm{c},i}\mathrm{sign}(\omega_i) = \tau_i - \tau_{\mathrm{a},i}. \tag{17} $$

In which, for the wheel joint attached with ID i, $\mathcal{I}_i$ denotes its moment of inertia, $f_{\mathrm{v},i}$ and $f_{\mathrm{c},i}$ denote its viscous and Coulomb friction coefficients, τ_i is the actual joint driving torque, and $\tau_{\mathrm{a},i}$ is the torque output of the joint toward its corresponding wheel, which is $\tau_{\mathrm{a},i} = \boldsymbol{z}_{\mathrm{w}}^{\mathrm{T}}\, {}^{\mathrm{W}_i}\boldsymbol{F}$.

According to Fig. 2, the velocity vector of the MP body can be expressed as

$$ {}^{\mathrm{P_c}}\boldsymbol{V} = {}^{\mathrm{P_p}}\boldsymbol{U}_{\mathrm{P_c}}^{\mathrm{T}}\, {}^{\mathrm{P_p}}\boldsymbol{V} = {}^{\mathrm{A}_i}\boldsymbol{U}_{\mathrm{P_c}}^{\mathrm{T}}\, {}^{\mathrm{A}_i}\boldsymbol{V}, \tag{18} $$

and its dynamic model can be calculated as

$$ {}^{\mathrm{P_c}}\boldsymbol{F}^{*} = {}^{\mathrm{P_c}}\boldsymbol{F} - {}^{\mathrm{P_c}}\boldsymbol{U}_{\mathrm{P_p}}\, {}^{\mathrm{P_p}}\boldsymbol{F} - \sum_i \left({}^{\mathrm{P_c}}\boldsymbol{U}_{\mathrm{A}_i}\, {}^{\mathrm{A}_i}\boldsymbol{F} \right), \tag{19} $$

where ${}^{\mathrm{P_c}}\boldsymbol{F} \in \mathbb{R}^6$ denotes the F/T vector applied from the virtual manipulator to the MP body, which is obviously ${}^{\mathrm{P_c}}\boldsymbol{F} = \boldsymbol{0}$.

In summary, the dynamics of the manipulator are shown in (9) and (10), the dynamics of the MP are presented in (14)$\sim$(17) and (19), and their dynamics connection can be resolved by (11).

III. Virtual Decomposition Control of Wheeled Mobile Manipulators

The main target of this section is to design an appropriate algorithm to realize task-space trajectory tracking for a complex WMM via the VDC framework. We are starting with the presentation of controlling the EE in Section III-A. Then, adaptive controllers of the manipulator (including the links and joints) and the MP (including the wheels, wheel joints, and MP body) are designed in Sections III-B and III-C, respectively.

A. Control of End-effector

The linear/angular velocity vector ${}^{\mathrm{C}}\boldsymbol{V}_{\mathrm{e}} \in \mathbb{R}^6$ of the contact point in frame $\{\mathrm{C}\}$ can be written as

$$ {}^{\mathrm{C}}\boldsymbol{V}_{\mathrm{e}} = \boldsymbol{T}\dot{\boldsymbol{x}}_{\mathrm{e}} \tag{20} $$

with $\boldsymbol{T} \in \mathbb{R}^{6\times r}$ denoting a transformation matrix to connect the velocity of the EE in $\{\Sigma_{\mathrm{w}}\}$ and the velocity of the contact point in $\{\mathrm{C}\}$, which can be expressed as $\boldsymbol{T} = \left[\boldsymbol{I}_r,\, \boldsymbol{0}_{r\times(6-r)}\right]^{\mathrm{T}}$. $\boldsymbol{I}_r$ denotes the identity matrix of dimension r, and $\boldsymbol{T}^{\mathrm{T}}\,\boldsymbol{T} = \boldsymbol{I}_r$ is ensured. Then, the velocity vector of the EE in its own frame can be obtained using (4f).

The F/T vector of the contact point expressed in $\{\mathrm{C}\}$ is derived as

$$ {}^{\mathrm{C}}\boldsymbol{F}_{\mathrm{e}} = \boldsymbol{T}\boldsymbol{f}_{\mathrm{e}}, \tag{21} $$

where $\boldsymbol{f}_{\mathrm{e}} \in \mathbb{R}^r$ represents the robot-environment interaction force vector in the same dimension as $\dot{\boldsymbol{x}}_{\mathrm{e}}$. Thus, the driving F/T vector of the EE, ${}^{\mathrm{T}_{\mathrm{EE}}}\boldsymbol{F}$, can be derived using (9a). Here, like (16), let $\boldsymbol{f}_{\mathrm{e}}$ be expressed in a linear parameterization form as $\boldsymbol{f}_{\mathrm{e}} = \boldsymbol{Y}_{\mathrm{e}}\boldsymbol{\theta}_{\mathrm{e}}$.

The terminology of required velocity is an essential concept in the VDC approach, including the desired velocity and one or more terms related to the control errors, such as position errors and/or force errors. The control objective of this manuscript is to make the WMM's actual position trajectory track its desired position trajectory.

Then, for the EE, similar to (20), the required velocity of the contact point in $\{\mathrm{C}\}$ is expressed as

$$ {}^{\mathrm{C}}\boldsymbol{V}_{\mathrm{r}} = \boldsymbol{T}\dot{\boldsymbol{x}}_{\mathrm{r}} \tag{22} $$

with $\dot{\boldsymbol{x}}_{\mathrm{r}} \in \mathbb{R}^r$ denoting the required contact point velocity vector, which is expressed as

$$ \dot{\boldsymbol{x}}_{\mathrm{r}} = \dot{\boldsymbol{x}}_{\mathrm{d}} + \boldsymbol{\Lambda}(\boldsymbol{x}_{\mathrm{d}} - \boldsymbol{x}_{\mathrm{e}}), \tag{23} $$

where $\boldsymbol{x}_{\mathrm{d}} \in \mathbb{R}^r$ is the desired EE trajectory at the contact point and $\boldsymbol{\Lambda} \in \mathbb{R}^{r\times r}$ is a diagonal positive-definite matrix. Then, the required velocity of the EE in its own frame is

$$ {}^{\mathrm{EE}}\boldsymbol{V}_{\mathrm{r}} = {}^{\mathrm{C}}\boldsymbol{U}_{\mathrm{EE}}^{\mathrm{T}}\, {}^{\mathrm{C}}\boldsymbol{V}_{\mathrm{r}}. \tag{24} $$

Similar to (21), the required F/T of the contact point in $\{\mathrm{C}\}$ can be expressed as

$$ {}^{\mathrm{C}}\boldsymbol{F}_{\mathrm{r}} = \boldsymbol{T}\hat{\boldsymbol{f}}_{\mathrm{e}}, \tag{25} $$

where $\hat{\boldsymbol{f}}_{\mathrm{e}} \in \mathbb{R}^r$ denotes the desired task-space force vector of the EE, with

$$ \hat{\boldsymbol{f}}_{\mathrm{e}} = \boldsymbol{Y}_{\mathrm{e}}\hat{\boldsymbol{\theta}}_{\mathrm{e}}. \tag{26} $$

The following projection function in [38] is utilized for unknown parameter adaptation.

Definition 2. *A projection function $\mathcal{P}(s(t), k, a(t), b(t), t) \in \mathbb{R}$ is a differentiable scalar function defined in $t \geqslant 0$ such that its time derivative is governed by*

$$ \dot{\mathcal{P}} = ks(t)\kappa \tag{27} $$

with

$$ \kappa = \begin{cases} 0, & \text{if } \mathcal{P} \leqslant a(t) \text{ and } s(t) \leqslant 0 \\ 0, & \text{if } \mathcal{P} \geqslant b(t) \text{ and } s(t) \geqslant 0 \\ 1, & \text{otherwise} \end{cases} $$

where $s(t) \in \mathbb{R}$ is a scalar variable, k is a positive constant and $a(t) \leqslant b(t)$ holds.

Consider an arbitrary $\mathcal{P}$ function defined in (27), and for any constant $\mathcal{P}_{\mathrm{c}}$ satisfying $a(t) \leqslant \mathcal{P}_{\mathrm{c}} \leqslant b(t)$, it follows that

$$ (\mathcal{P}_{\mathrm{c}} - \mathcal{P})\left(s(t) - \frac{1}{k}\dot{\mathcal{P}}\right) \leqslant 0. \tag{28} $$

By defining

$$ \boldsymbol{s}_{\mathrm{e}} = \boldsymbol{Y}_{\mathrm{e}}^{\mathrm{T}}(\dot{\boldsymbol{x}}_{\mathrm{r}} - \dot{\boldsymbol{x}}), \tag{29} $$

each element of $\hat{\boldsymbol{\theta}}_{\mathrm{e}}$ in (26) can be updated by employing (27) as

$$ \hat{\theta}_{\mathrm{e}\gamma} = \mathcal{P}(s_{\mathrm{e}\gamma}, \rho_{\mathrm{e}\gamma}, \underline{\theta}_{\mathrm{e}\gamma}, \overline{\theta}_{\mathrm{e}\gamma}, t), \tag{30} $$

where $\hat{\theta}_{\mathrm{e}\gamma}$ is the γ^{th} element of $\hat{\boldsymbol{\theta}}_{\mathrm{e}}$, $s_{\mathrm{e}\gamma}$ is the γ^{th} element of $\boldsymbol{s}_{\mathrm{e}}$, $\rho_{\mathrm{e}\gamma} > 0$ is the update gain, and $\underline{\theta}_{\mathrm{e}\gamma}$ and $\overline{\theta}_{\mathrm{e}\gamma}$ are the lower bound and the upper bound of $\theta_{\mathrm{e}\gamma}$.

The required net F/T vector of the EE can be expressed as

$$ {}^{\mathrm{EE}}\boldsymbol{F}_{\mathrm{r}}^{*} = \boldsymbol{Y}_{\mathrm{EE}}\hat{\boldsymbol{\theta}}_{\mathrm{EE}} + \boldsymbol{K}_{\mathrm{EE}}({}^{\mathrm{EE}}\boldsymbol{V}_{\mathrm{r}} - {}^{\mathrm{EE}}\boldsymbol{V}) \tag{31} $$

with

$$ \boldsymbol{Y}_{\mathrm{EE}}\boldsymbol{\theta}_{\mathrm{EE}} = \boldsymbol{M}_{\mathrm{EE}}\frac{\mathrm{d}}{\mathrm{d}t}({}^{\mathrm{EE}}\boldsymbol{V}_{\mathrm{r}}) + \boldsymbol{C}_{\mathrm{EE}}({}^{\mathrm{EE}}\boldsymbol{\omega}){}^{\mathrm{EE}}\boldsymbol{V}_{\mathrm{r}} + \boldsymbol{G}_{\mathrm{EE}}, $$

where $\boldsymbol{Y}_{\mathrm{EE}} \in \mathbb{R}^{6\times 13}$ is a regressor matrix, $\boldsymbol{\theta}_{\mathrm{EE}} \in \mathbb{R}^{13}$ and $\hat{\boldsymbol{\theta}}_{\mathrm{EE}} \in \mathbb{R}^{13}$ are the unknown parameter vector and its estimate, respectively, and $\boldsymbol{K}_{\mathrm{EE}} \in \mathbb{R}^{6\times 6}$ is a symmetric positive-definite matrix, representing the velocity feedback control gain. $\boldsymbol{Y}_{\mathrm{EE}}$ is a function of the known parameters (measured or calculated), including $\frac{\mathrm{d}}{\mathrm{d}t}({}^{\mathrm{EE}}\boldsymbol{V}_{\mathrm{r}})$, ${}^{\mathrm{EE}}\boldsymbol{V}_{\mathrm{r}}$, and ${}^{\mathrm{EE}}\boldsymbol{V}$. $\boldsymbol{\theta}_{\mathrm{EE}}$ denotes a function of the unknown parameters, containing EE's mass, position of the mass center, and moment of inertia. The exact representation of each element of these parameters can be found in [38].

The estimated parameters of $\hat{\boldsymbol{\theta}}_{\mathrm{EE}}$ in (31) can be updated using the parameter adaptation method provided in Definition 2 with

$$ \boldsymbol{s}_{\mathrm{EE}} = \boldsymbol{Y}_{\mathrm{EE}}^{\mathrm{T}}({}^{\mathrm{EE}}\boldsymbol{V}_{\mathrm{r}} - {}^{\mathrm{EE}}\boldsymbol{V}). \tag{32} $$

Then, each element of $\hat{\boldsymbol{\theta}}_{\mathrm{EE}}$ can be updated using (27) as

$$ \hat{\theta}_{\mathrm{EE}\gamma} = \mathcal{P}(s_{\mathrm{EE}\gamma}, \rho_{\mathrm{EE}\gamma}, \underline{\theta}_{\mathrm{EE}\gamma}, \overline{\theta}_{\mathrm{EE}\gamma}, t),\ \forall \gamma \in [1, 13], \tag{33} $$

where $\hat{\theta}_{\mathrm{EE}\gamma}$ is the γ^{th} element of $\hat{\boldsymbol{\theta}}_{\mathrm{EE}}$, $s_{\mathrm{EE}\gamma}$ is the γ^{th} element of $\boldsymbol{s}_{\mathrm{EE}}$, $\rho_{\mathrm{EE}\gamma} > 0$ is the update gain, and $\underline{\theta}_{\mathrm{EE}\gamma}$ and $\overline{\theta}_{\mathrm{EE}\gamma}$ are the lower bound and the upper bound of $\theta_{\mathrm{EE}\gamma}$.

Similar to (9a), the required net F/T vector of the EE can be calculated as

$$ {}^{\mathrm{EE}}\boldsymbol{F}_{\mathrm{r}}^{*} = {}^{\mathrm{EE}}\boldsymbol{U}_{\mathrm{T}_{\mathrm{EE}}}\, {}^{\mathrm{T}_{\mathrm{EE}}}\boldsymbol{F}_{\mathrm{r}} - {}^{\mathrm{EE}}\boldsymbol{U}_{\mathrm{C}}\, {}^{\mathrm{C}}\boldsymbol{F}_{\mathrm{r}}. \tag{34} $$

B. Control of Multi-DoF Manipulators

The linear/angular velocity vector of the i^{th} link ${}^{\mathrm{B}_i}\boldsymbol{V} \in \mathbb{R}^6$ can be obtained using (4a)∼(4c), and its F/T vector ${}^{\mathrm{B}_i}\boldsymbol{F} \in \mathbb{R}^6$ can be derived using (9b)∼(9d).

According to (7), the required joint velocity of the manipulator $\dot{q}_{\mathrm{m},i\mathrm{r}}$ can be calculated as

$$ \boldsymbol{v}_{\mathrm{r}} = \left[\boldsymbol{v}_{\mathrm{p,r}}^{\mathrm{T}},\ \dot{\boldsymbol{q}}_{\mathrm{m,r}}^{\mathrm{T}}\right]^{\mathrm{T}} = \boldsymbol{J}^{\dagger}\dot{\boldsymbol{x}}_{\mathrm{r}}, \tag{35} $$

where $(.)^{\dagger}$ denotes the Moore-Penrose pseudoinverse of a matrix[1]. The required velocity vector of the i^{th} link ${}^{\mathrm{B}_i}\boldsymbol{V}_{\mathrm{r}} \in \mathbb{R}^6$ is expressed as

$$ {}^{\mathrm{B}_1}\boldsymbol{V}_{\mathrm{r}} = \boldsymbol{z}\dot{q}_{\mathrm{m,1r}}, \tag{36a} $$

$$ {}^{\mathrm{T}_i}\boldsymbol{V}_{\mathrm{r}} = {}^{\mathrm{B}_{i-1}}\boldsymbol{U}_{\mathrm{T}_i}^{\mathrm{T}}\, {}^{\mathrm{B}_{i-1}}\boldsymbol{V}_{\mathrm{r}}, \tag{36b} $$

$$ {}^{\mathrm{B}_i}\boldsymbol{V}_{\mathrm{r}} = \boldsymbol{z}\dot{q}_{\mathrm{m},i\mathrm{r}} + {}^{\mathrm{T}_i}\boldsymbol{U}_{\mathrm{B}_i}^{\mathrm{T}}\, {}^{\mathrm{T}_i}\boldsymbol{V}_{\mathrm{r}} = \boldsymbol{z}\dot{q}_{\mathrm{m},i\mathrm{r}} + {}^{\mathrm{B}_{i-1}}\boldsymbol{U}_{\mathrm{B}_i}^{\mathrm{T}}\, {}^{\mathrm{B}_{i-1}}\boldsymbol{V}_{\mathrm{r}}, \tag{36c} $$

[1] The last m elements of $\boldsymbol{v}$ denote the joint velocities of the manipulator, and we use $\dot{\boldsymbol{q}}_{\mathrm{m}}$ to refer to them, since they are equal to each other.

The required F/T vector of the i^{th} link ${}^{\mathrm{B}_i}\boldsymbol{F} \in \mathbb{R}^6$ can be obtained as

$$
\begin{aligned}
{}^{\mathrm{B}_m}\boldsymbol{F}_{\mathrm{r}}^{*} &= {}^{\mathrm{B}_m}\boldsymbol{F}_{\mathrm{r}} - {}^{\mathrm{B}_m}\boldsymbol{U}_{\mathrm{T}_{\mathrm{EE}}}{}^{\mathrm{T}_{\mathrm{EE}}}\boldsymbol{F}_{\mathrm{r}}, &\text{(37a)}\\
{}^{\mathrm{T}_i}\boldsymbol{F}_{\mathrm{r}} &= {}^{\mathrm{T}_i}\boldsymbol{U}_{\mathrm{B}_i}{}^{\mathrm{B}_i}\boldsymbol{F}_{\mathrm{r}}, \quad i = m, \dots, 2, &\text{(37b)}\\
{}^{\mathrm{B}_i}\boldsymbol{F}_{\mathrm{r}}^{*} &= {}^{\mathrm{B}_i}\boldsymbol{F}_{\mathrm{r}} - {}^{\mathrm{B}_i}\boldsymbol{U}_{\mathrm{T}_{i+1}}{}^{\mathrm{T}_{i+1}}\boldsymbol{F}_{\mathrm{r}}, \quad i = m-1, \dots, 1, &\text{(37c)}
\end{aligned}
$$

The VDC-based control procedure of the links is the same as the process of the EE in (31) and (32)∼(34) with appropriate frame substitutions.

After that, the controller of the manipulator joints is presented. The relationship between the joint velocity vector and the linear/angular velocity vector of the adjacent links is shown in (4a)∼(4c). The dynamics of the i^{th} joint are provided by (10). Combined with (37), the command joint torque of the i^{th} manipulator joint is designed as [25]

$$
\begin{cases}
\tau_{\mathrm{t},id} = \boldsymbol{Y}_{\mathrm{q}i}\hat{\boldsymbol{\theta}}_{\mathrm{q}i} + \boldsymbol{z}^{\mathrm{T}}\,{}^{\mathrm{B}_i}\boldsymbol{F}_{\mathrm{r}} + k_{\mathrm{vq},i}(\dot{q}_{\mathrm{m},i\mathrm{r}} - \dot{q}_{\mathrm{m},i}),\\
\phi_{\mathrm{m},i\mathrm{r}} = \tau_{\mathrm{t},id}/\hat{k}_{\mathrm{f},i} + q_{\mathrm{m},i\mathrm{r}},\\
\tau_i = \tau_{\mathrm{t},id} + \boldsymbol{Y}_{\phi i}\hat{\boldsymbol{\theta}}_{\phi i} + k_{\mathrm{v}\phi,i}(\dot{\phi}_{\mathrm{m},i\mathrm{r}} - \dot{\phi}_{\mathrm{m},i}),\\
\boldsymbol{Y}_{\mathrm{q}i} = \left[\dot{q}_{\mathrm{m},i\mathrm{r}}, \mathrm{sign}(\dot{q}_{\mathrm{m},i\mathrm{r}})\right],\\
\boldsymbol{\theta}_{\mathrm{q}i} = [f_{\mathrm{vq},i}, f_{\mathrm{cq},i}]^{\mathrm{T}},\\
\boldsymbol{Y}_{\phi i} = \left[\ddot{\phi}_{\mathrm{m},i\mathrm{r}}, \dot{\phi}_{\mathrm{m},i\mathrm{r}}, \mathrm{sign}(\dot{\phi}_{\mathrm{m},i\mathrm{r}})\right],\\
\boldsymbol{\theta}_{\phi i} = [\mathcal{I}_{\mathrm{m},i}, f_{\mathrm{v}\phi,i}, f_{\mathrm{c}\phi,i}]^{\mathrm{T}},
\end{cases}
\tag{38}
$$

where $k_{\mathrm{vq},i}$ and $k_{\mathrm{v}\phi,i}$ are two positive constants, representing the link-side and motor-side control gains of the i^{th} joint, respectively.

Define

$$
\begin{cases}
\boldsymbol{s}_{\mathrm{q}i} = \boldsymbol{Y}_{\mathrm{q}i}^{\mathrm{T}}(\dot{q}_{\mathrm{m},i\mathrm{r}} - \dot{q}_{\mathrm{m},i}),\\
\boldsymbol{s}_{\phi i} = \boldsymbol{Y}_{\phi i}^{\mathrm{T}}(\dot{\phi}_{\mathrm{m},i\mathrm{r}} - \dot{\phi}_{\mathrm{m},i}),\\
s_{\mathrm{kf}i} = \left(\phi_{\mathrm{m},i\mathrm{r}} - q_{\mathrm{m},i\mathrm{r}}\right)\left[(\dot{\phi}_{\mathrm{m},i\mathrm{r}} - \dot{\phi}_{\mathrm{m},i}) - (\dot{q}_{\mathrm{m},i\mathrm{r}} - \dot{q}_{\mathrm{m},i})\right],
\end{cases}
\tag{39}
$$

then, each element of $\hat{\boldsymbol{\theta}}_{\mathrm{q}i}$, $\hat{\boldsymbol{\theta}}_{\phi i}$, and $\hat{k}_{\mathrm{f},i}$ can be updated using (27), respectively, as

$$
\begin{cases}
\hat{\theta}_{\mathrm{q}i\gamma} = \mathcal{P}(s_{\mathrm{q}i\gamma}, \rho_{\mathrm{q}i\gamma}, \underline{\theta}_{\mathrm{q}i\gamma}, \overline{\theta}_{\mathrm{q}i\gamma}, t), \quad \forall\gamma \in \{1, 2\},\\
\hat{\theta}_{\phi i\gamma} = \mathcal{P}(s_{\phi i\gamma}, \rho_{\phi i\gamma}, \underline{\theta}_{\phi i\gamma}, \overline{\theta}_{\phi i\gamma}, t), \quad \forall\gamma \in \{1, 2, 3\},\\
\hat{k}_{\mathrm{f},i} = \mathcal{P}(s_{\mathrm{kf}i}, \rho_{\mathrm{kf}i}, \underline{k}_{\mathrm{f},i}, \overline{k}_{\mathrm{f},i}, t),
\end{cases}
\tag{40}
$$

where $\hat{\theta}_{\mathrm{q}i\gamma}$, $\hat{\theta}_{\phi i\gamma}$, $s_{\mathrm{q}i\gamma}$, and $s_{\phi i\gamma}$ represent the γ^{th} element of $\hat{\boldsymbol{\theta}}_{\mathrm{q}i}$, $\hat{\boldsymbol{\theta}}_{\phi i}$, $\boldsymbol{s}_{\mathrm{q}i}$, and $\boldsymbol{s}_{\phi i}$, respectively; $\rho_{\mathrm{q}i\gamma}$, $\rho_{\phi i\gamma}$, and $\rho_{\mathrm{kf}i}$ denote positive parameter update gains; $\underline{\theta}_{\mathrm{q}i\gamma}$ and $\overline{\theta}_{\mathrm{q}i\gamma}$ denote the lower and upper bounds of $\theta_{\mathrm{q}i\gamma}$; $\underline{\theta}_{\phi i\gamma}$ and $\overline{\theta}_{\phi i\gamma}$ represent the lower and upper bounds of $\theta_{\phi i\gamma}$; and $\underline{k}_{\mathrm{f},i}$ and $\overline{k}_{\mathrm{f},i}$ are the lower and upper bounds of $k_{\mathrm{f},i}$.

C. Control of Wheeled Mobile Platform

According to Fig. 1, (11) and (37), we can calculate the required F/T applied to the MP by the manipulator, which is noted as ${}^{\mathrm{P_P}}\boldsymbol{F}_{\mathrm{r}}$.

In line with (12), the required velocity of the wheel with ID i can be designed as

$$
{}^{\mathrm{W}_i}\boldsymbol{V}_{\mathrm{r}} = \boldsymbol{z}_{\mathrm{w}}\omega_{i\mathrm{r}} + {}^{\mathrm{A}_i}\boldsymbol{U}_{\mathrm{W}_i}^{\mathrm{T}}\,{}^{\mathrm{A}_i}\boldsymbol{V}_{\mathrm{r}}, \tag{41}
$$

where $i \in \{\mathrm{fl}, \mathrm{fr}, \mathrm{bl}, \mathrm{br}\}$ denotes the wheel ID, the required velocity of the wheels $\omega_{i\mathrm{r}}$ can be obtained via (35), and ${}^{\mathrm{A}_i}\boldsymbol{V}_{\mathrm{r}}$ can be derived through matrix transformation using ${}^{\mathrm{P_c}}\boldsymbol{V}_{\mathrm{r}}$. Combined with (13), the required velocity of each wheel at the contact point can be designed as

$$
{}^{\mathrm{C}_i}\boldsymbol{V}_{\mathrm{wg,r}} = {}^{\mathrm{W}_i}\boldsymbol{U}_{\mathrm{C}_i}^{\mathrm{T}}\,{}^{\mathrm{W}_i}\boldsymbol{V}_{\mathrm{r}} = \boldsymbol{T}_{\mathrm{c},i}\boldsymbol{\chi}_{i,\mathrm{r}}, \tag{42}
$$

here, it is worth mentioning that $\boldsymbol{\chi}_{i,\mathrm{r}} \in \mathbb{R}^{6-n_{\mathrm{wg},i}}$ is not necessarily an independent variable, it can also be derived from the required velocity of the wheel ${}^{\mathrm{W}_i}\boldsymbol{V}_{\mathrm{r}}$.

Similar to (31), the net F/T vector of each wheel is designed as

$$
{}^{\mathrm{W}_i}\boldsymbol{F}_{\mathrm{r}}^{*} = \boldsymbol{Y}_{\mathrm{W}_i}\hat{\boldsymbol{\theta}}_{\mathrm{W}_i} + \boldsymbol{K}_{\mathrm{W}_i}({}^{\mathrm{W}_i}\boldsymbol{V}_{\mathrm{r}} - {}^{\mathrm{W}_i}\boldsymbol{V}), \tag{43}
$$

where the calculation of unknown parameter vector $\hat{\boldsymbol{\theta}}_{\mathrm{W}_i}$ is similar to (32) and (33) with appropriate frame substitutions, and $\boldsymbol{K}_{\mathrm{W}_i} \in \mathbb{R}^{6\times 6}$ is a symmetric positive-definite matrix, representing the velocity feedback control gain. Combined with wheel dynamic model (14), we can derive

$$
\begin{aligned}
{}^{\mathrm{W}_i}\boldsymbol{F}_{\mathrm{r}} &= {}^{\mathrm{W}_i}\boldsymbol{F}_{\mathrm{r}}^{*} + {}^{\mathrm{W}_i}\boldsymbol{U}_{\mathrm{C}_i}{}^{\mathrm{C}_i}\boldsymbol{F}_{\mathrm{wg,r}}, &\text{(44a)}\\
{}^{\mathrm{A}_i}\boldsymbol{F}_{\mathrm{r}} &= {}^{\mathrm{A}_i}\boldsymbol{U}_{\mathrm{W}_i}{}^{\mathrm{W}_i}\boldsymbol{F}_{\mathrm{r}}. &\text{(44b)}
\end{aligned}
$$

Then, the required F/T vector of the contact point should be calculated. According to (15) and (16), the required F/T vector of the contact point in frame $\{\mathrm{C}\}$ can be designed as

$$
{}^{\mathrm{C}_i}\boldsymbol{F}_{\mathrm{wg,r}} = \boldsymbol{T}_{\mathrm{c},i}\boldsymbol{Y}_{\mathrm{c},i}\hat{\boldsymbol{\theta}}_{\mathrm{c},i} + \boldsymbol{T}_{\mathrm{f},i}\boldsymbol{\varphi}_{i,\mathrm{d}}, \tag{45}
$$

where $\boldsymbol{\varphi}_{i,\mathrm{d}} \in \mathbb{R}^{n_{\mathrm{wg},i}}$ denotes the desired value of the required F/T vector. To estimate $\hat{\boldsymbol{\theta}}_{\mathrm{c},i}$, we set $\boldsymbol{s}_{\mathrm{c},i} = \boldsymbol{Y}_{\mathrm{c},i}^{\mathrm{T}}(\boldsymbol{\chi}_{i,\mathrm{r}} - \boldsymbol{\chi}_i)$, and each element of $\hat{\boldsymbol{\theta}}_{\mathrm{c},i}$ can be evaluated according to (27).

The joint of the wheel is rigid, and its dynamic model is shown in (17). Then, combined with (44), the command torque of the wheel joint with ID i is designed as

$$
\begin{cases}
\tau_i = \boldsymbol{Y}_{\mathrm{A}_i}\hat{\boldsymbol{\theta}}_{\mathrm{A}_i} + \boldsymbol{z}_{\mathrm{w}}^{\mathrm{T}}\,{}^{\mathrm{A}_i}\boldsymbol{F}_{\mathrm{r}} + k_{\mathrm{A}_i}(\omega_{i\mathrm{r}} - \omega_i),\\
\boldsymbol{Y}_{\mathrm{A}_i} = \left[\dot{\omega}_{i\mathrm{r}}, \omega_{i\mathrm{r}}, \mathrm{sign}(\omega_{i\mathrm{r}})\right],\\
\boldsymbol{\theta}_{\mathrm{A}_i} = [\mathcal{I}_i, f_{\mathrm{v},i}, f_{\mathrm{c},i}]^{\mathrm{T}},
\end{cases}
\tag{46}
$$

where k_{A_i} is a positive constant, representing the control gain of the wheel joint with ID i.

Define

$$
\boldsymbol{s}_{\mathrm{A}_i} = \boldsymbol{Y}_{\mathrm{A}_i}^{\mathrm{T}}(\omega_{i\mathrm{r}} - \omega_i), \tag{47}
$$

then, each element of $\hat{\boldsymbol{\theta}}_{\mathrm{A}_i}$ can be updated using (27), respectively, as

$$
\hat{\theta}_{\mathrm{A}_i\gamma} = \mathcal{P}(s_{\mathrm{A}_i\gamma}, \rho_{\mathrm{A}_i\gamma}, \underline{\theta}_{\mathrm{A}_i\gamma}, \overline{\theta}_{\mathrm{A}_i\gamma}, t), \quad \forall\gamma \in \{1, 2, 3\}, \tag{48}
$$

where $s_{\mathrm{A}_i\gamma}$ represents the γ^{th} element of $\boldsymbol{s}_{\mathrm{A}_i}$, $\rho_{\mathrm{A}_i\gamma}$ denotes a positive parameter update gain, $\underline{\theta}_{\mathrm{A}_i\gamma}$ and $\overline{\theta}_{\mathrm{A}_i\gamma}$ denote the lower and upper bounds of $\theta_{\mathrm{A}_i\gamma}$, respectively.

According to the kinematic model of the MP, as shown in (18), its required velocity meets the following condition

$$
{}^{\mathrm{P_c}}\boldsymbol{V}_{\mathrm{r}} = {}^{\mathrm{P_P}}\boldsymbol{U}_{\mathrm{P_c}}^{\mathrm{T}}\,{}^{\mathrm{P_P}}\boldsymbol{V}_{\mathrm{r}} = {}^{\mathrm{A}_i}\boldsymbol{U}_{\mathrm{P_c}}^{\mathrm{T}}\,{}^{\mathrm{A}_i}\boldsymbol{V}_{\mathrm{r}}. \tag{49}
$$

Then, similar to (31) and (32)∼(34), the required net F/T vector of the MP ${}^{\mathrm{P_c}}\boldsymbol{F}_{\mathrm{r}}^{*}$ can be calculated. Combined with (19), the required F/T vector of the MP can be derived as

$$
{}^{\mathrm{P_c}}\boldsymbol{F}_{\mathrm{r}} = {}^{\mathrm{P_c}}\boldsymbol{F}_{\mathrm{r}}^{*} + {}^{\mathrm{P_c}}\boldsymbol{U}_{\mathrm{P_P}}{}^{\mathrm{P_P}}\boldsymbol{F}_{\mathrm{r}} + \sum_i \left({}^{\mathrm{P_c}}\boldsymbol{U}_{\mathrm{A}_i}{}^{\mathrm{A}_i}\boldsymbol{F}_{\mathrm{r}}\right). \tag{50}
$$

The massless virtual manipulator must ensure that its force vector transmitted to the MP body meets ${}^{\mathrm{P_c}}\boldsymbol{F} = \mathbf{0}$. Thus, the required F/T vector of the virtual manipulator is designed as

$$ {}^{\mathrm{P_c}}\boldsymbol{F}_{\mathrm{r}} = -\boldsymbol{K}_{\mathrm{vm}}({}^{\mathrm{P_c}}\boldsymbol{V}_{\mathrm{r}} - {}^{\mathrm{P_c}}\boldsymbol{V}), \tag{51} $$

where $\boldsymbol{K}_{\mathrm{vm}} \in \mathbb{R}^{6\times 6}$ is a semi-definite matrix, representing the velocity feedback control gain. It is noteworthy that (51) contains the condition that ${}^{\mathrm{P_c}}\boldsymbol{F}_{\mathrm{r}} = \mathbf{0}$, since $\boldsymbol{K}_{\mathrm{vm}} = \mathbf{0}$ is allowed.

The entire control system is shown in Fig. 3.

IV. Stability Analysis

We present the stability proof of our control approach in this section. Sections IV-A, IV-B, and IV-C provide the *virtual stability* of the EE, multi-DoF manipulators, and MP, respectively. Section IV-D proves the stability of the entire WMM system based on the *virtual stability* of each subsystem. The computational complexity analysis of the proposed method is presented in Section IV-E.

In the beginning, the concept of VPF and *virtual stability* is presented. One of the unique features of the VDC approach is the introduction of VPF, which is defined in Definition 3. The VPF describes the dynamic interactions among the subsystems, which is essential for the proof of *virtual stability*, and will be presented in Definition 4.

Definition 3. *Consider a rigid body attached with a frame* $\{\mathrm{A}\}$*, with respect to this frame, the VPF is defined as the inner product of the linear/angular velocity vector error and the F/T vector error, that is*

$$ p_{\mathrm{A}} \overset{def}{=} ({}^{\mathrm{A}}\boldsymbol{V}_{\mathrm{r}} - {}^{\mathrm{A}}\boldsymbol{V})^{\mathrm{T}}({}^{\mathrm{A}}\boldsymbol{F}_{\mathrm{r}} - {}^{\mathrm{A}}\boldsymbol{F}), \tag{52} $$

where ${}^{\mathrm{A}}\boldsymbol{V}_{\mathrm{r}} \in \mathbb{R}^6$ *and* ${}^{\mathrm{A}}\boldsymbol{F}_{\mathrm{r}} \in \mathbb{R}^6$ *represent the required vectors of* ${}^{\mathrm{A}}\boldsymbol{V} \in \mathbb{R}^6$ *and* ${}^{\mathrm{A}}\boldsymbol{F} \in \mathbb{R}^6$*, respectively.*

Definition 4. *A subsystem with a driven VCP to which frame* $\{\mathrm{A}\}$ *is attached and a driving VCP to which frame* $\{\mathrm{C}\}$ *is attached is said to be virtually stable with its affiliated vector* $\boldsymbol{x}(t)$ *being a virtual function in* L_∞ *and its affiliated vector* $\boldsymbol{y}(t)$ *being a virtual function in* L_2 *, if and only if there exists a nonnegative accompanying function*

$$ \nu(t) \geqslant \frac{1}{2}\boldsymbol{x}(t)^{\mathrm{T}}\boldsymbol{P}\boldsymbol{x}(t), \tag{53} $$

such that

$$ \dot{\nu}(t) \leqslant -\boldsymbol{y}(t)^{\mathrm{T}}\boldsymbol{Q}\boldsymbol{y}(t) + p_{\mathrm{A}} - p_{\mathrm{C}} - s(t), \tag{54} $$

which is subject to

$$ \int_0^\infty s(t)\mathrm{d}t \geqslant -\gamma_s \tag{55} $$

with $0 \leqslant \gamma_s < \infty$*, where* $\boldsymbol{P}$ *and* $\boldsymbol{Q}$ *are two positive-definite matrices.*

A. Virtual Stability of End-effector

Theorem 1. *Consider the EE described by (8), (9a), (20), (21), combined with its respective control equations (22)∼(31), (34), and with the parameter adaptation algorithms (32) and (33). Then, the EE is virtually stable.*

Proof. Define the nonnegative accompanying function for the EE ν_{EE} as

$$ \begin{aligned} \nu_{\mathrm{EE}} = &\frac{1}{2}({}^{\mathrm{EE}}\boldsymbol{V}_{\mathrm{r}} - {}^{\mathrm{EE}}\boldsymbol{V})^{\mathrm{T}}\boldsymbol{M}_{\mathrm{EE}}({}^{\mathrm{EE}}\boldsymbol{V}_{\mathrm{r}} - {}^{\mathrm{EE}}\boldsymbol{V}) + \\ &\frac{1}{2}\sum_{\gamma=1}^{13}\frac{\left(\theta_{\mathrm{EE}\gamma} - \hat{\theta}_{\mathrm{EE}\gamma}\right)^2}{\rho_{\mathrm{EE}\gamma}}, \end{aligned} \tag{56} $$

then, the time derivative of (56) can be derived as

$$ \dot{\nu}_{\mathrm{EE}} \leqslant -({}^{\mathrm{EE}}\boldsymbol{V}_{\mathrm{r}} - {}^{\mathrm{EE}}\boldsymbol{V})^{\mathrm{T}}\boldsymbol{K}_{\mathrm{EE}}({}^{\mathrm{EE}}\boldsymbol{V}_{\mathrm{r}} - {}^{\mathrm{EE}}\boldsymbol{V}) + p_{\mathrm{T_{EE}}} - p_{\mathrm{C}}, \tag{57} $$

where $p_{\mathrm{T_{EE}}}$ is the VPF (defined in Definition 3) at the driven VCP of the EE, and p_{C} is the VPF between the EE and the environment.

It should be noted that the EE only has one VCP (shown in Fig. 1), but two VPFs appear in (57). The VPF $p_{\mathrm{T_{EE}}}$ locates at the VCP attached to frame $\{\mathrm{T_{EE}}\}$ of the object. Therefore, for the *virtual stability* of the EE, the condition to guarantee that the existence of VPF p_{C} still satisfies Definition 4 must be found.

According to (20)∼ (26), (29)∼(30), and (52), it yields

$$ \begin{aligned} p_{\mathrm{C}} &= ({}^{\mathrm{C}}\boldsymbol{V}_{\mathrm{r}} - {}^{\mathrm{C}}\boldsymbol{V}_{\mathrm{e}})^{\mathrm{T}}({}^{\mathrm{C}}\boldsymbol{F}_{\mathrm{r}} - {}^{\mathrm{C}}\boldsymbol{F}_{\mathrm{e}}) \\ &= (\dot{\boldsymbol{x}}_{\mathrm{r}} - \dot{\boldsymbol{x}}_{\mathrm{e}})^{\mathrm{T}}\boldsymbol{T}^{\mathrm{T}}\boldsymbol{T}(\hat{\boldsymbol{f}}_e - \boldsymbol{f}_e) \\ &= -(\dot{\boldsymbol{x}}_{\mathrm{r}} - \dot{\boldsymbol{x}}_{\mathrm{e}})^{\mathrm{T}}\boldsymbol{Y}_{\mathrm{e}}(\boldsymbol{\theta}_{\mathrm{e}} - \hat{\boldsymbol{\theta}}_{\mathrm{e}}) \\ &= -\sum_\gamma\left(\theta_{\mathrm{e}\gamma} - \hat{\theta}_{\mathrm{e}\gamma}\right)\left[s_{\mathrm{e}\gamma} - \frac{\dot{\hat{\theta}}_{\mathrm{e}\gamma}}{\rho_{\mathrm{e}\gamma}}\right] - \sum_\gamma\left(\theta_{\mathrm{e}\gamma} - \hat{\theta}_{\mathrm{e}\gamma}\right)\frac{\dot{\hat{\theta}}_{\mathrm{e}\gamma}}{\rho_{\mathrm{e}\gamma}} \\ &\geqslant -\sum_\gamma\left(\theta_{\mathrm{e}\gamma} - \hat{\theta}_{\mathrm{e}\gamma}\right)\frac{\dot{\hat{\theta}}_{\mathrm{e}\gamma}}{\rho_{\mathrm{e}\gamma}}. \end{aligned} \tag{58} $$

Then, integrating (58) over time yields

$$ \begin{aligned} \int_0^\infty p_{\mathrm{C}}\mathrm{d}t &\geqslant \sum_\gamma\left[\frac{1}{2}\frac{\left(\theta_{\mathrm{e}\gamma} - \hat{\theta}_{\mathrm{e}\gamma}(t)\right)^2}{\rho_{\mathrm{e}\gamma}} - \frac{1}{2}\frac{\left(\theta_{\mathrm{e}\gamma} - \hat{\theta}_{\mathrm{e}\gamma}(0)\right)^2}{\rho_{\mathrm{e}\gamma}}\right] \\ &\geqslant -\sum_\gamma\frac{1}{2}\frac{\left(\theta_{\mathrm{e}\gamma} - \hat{\theta}_{\mathrm{e}\gamma}(0)\right)^2}{\rho_{\mathrm{e}\gamma}}. \end{aligned} \tag{59} $$

Therefore, the following condition

$$ \int_0^\infty p_{\mathrm{C}}\mathrm{d}t \geqslant -\gamma_{\mathrm{C}} \tag{60} $$

holds with $0 \leqslant \gamma_{\mathrm{C}} < \infty$. Then, the EE is *virtually stable* according to Definition 4. □

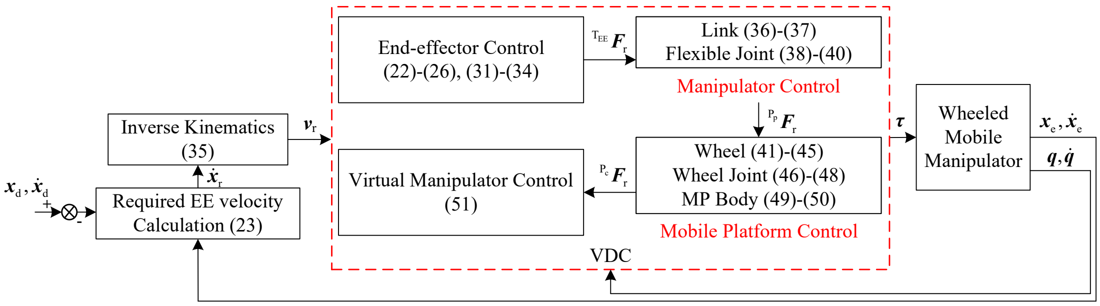

Figure 3: Block diagram of the proposed control system.

B. Virtual Stability of Multi-DoF Manipulators

We will first prove the *virtual stability* of the manipulator links, and followed by the *virtual stability* of its joints.

Theorem 2. *Consider the manipulator links described by* (4), (8), (9), *combined with their respective control equations* (36), (37), *and with parameter adaptation algorithms, which are the same as* (32) *and* (33) *with appropriate frame substitutions. Then, these links are virtually stable.*

Proof. Define the nonnegative accompanying function of the i^{th} link ν_{B_i} as

$$\begin{aligned}\nu_{\mathrm{B}_i} = &\frac{1}{2}({}^{\mathrm{B}_i}\boldsymbol{V}_{\mathrm{r}} - {}^{\mathrm{B}_i}\boldsymbol{V})^{\mathrm{T}}\boldsymbol{M}_{\mathrm{B}_i}({}^{\mathrm{B}_i}\boldsymbol{V}_{\mathrm{r}} - {}^{\mathrm{B}_i}\boldsymbol{V}) + \\ &\frac{1}{2}\sum_{\gamma=1}^{13}\frac{\left(\theta_{\mathrm{B}_i\gamma} - \hat{\theta}_{\mathrm{B}_i\gamma}\right)^2}{\rho_{\mathrm{B}_i\gamma}},\end{aligned} \tag{61}$$

then, the time derivative of (61) can be derived as

$$\begin{aligned}\dot{\nu}_{\mathrm{B}_i} \leqslant & -({}^{\mathrm{B}_i}\boldsymbol{V}_{\mathrm{r}} - {}^{\mathrm{B}_i}\boldsymbol{V})^{\mathrm{T}}\boldsymbol{K}_{\mathrm{B}_i}({}^{\mathrm{B}_i}\boldsymbol{V}_{\mathrm{r}} - {}^{\mathrm{B}_i}\boldsymbol{V}) + \\ &({}^{\mathrm{B}_i}\boldsymbol{V}_{\mathrm{r}} - {}^{\mathrm{B}_i}\boldsymbol{V})^{\mathrm{T}}({}^{\mathrm{B}_i}\boldsymbol{F}^*_{\mathrm{r}} - {}^{\mathrm{B}_i}\boldsymbol{F}^*).\end{aligned} \tag{62}$$

In view of (9), (37), and Definition 3, it yields

$$({}^{\mathrm{B}_m}\boldsymbol{V}_{\mathrm{r}} - {}^{\mathrm{B}_m}\boldsymbol{V})^{\mathrm{T}}({}^{\mathrm{B}_m}\boldsymbol{F}^*_{\mathrm{r}} - {}^{\mathrm{B}_m}\boldsymbol{F}^*) = p_{\mathrm{B}_m} - p_{\mathrm{T}_{\mathrm{EE}}}, \tag{63a}$$

$$({}^{\mathrm{B}_i}\boldsymbol{V}_{\mathrm{r}} - {}^{\mathrm{B}_i}\boldsymbol{V})^{\mathrm{T}}({}^{\mathrm{B}_i}\boldsymbol{F}^*_{\mathrm{r}} - {}^{\mathrm{B}_i}\boldsymbol{F}^*) = p_{\mathrm{B}_i} - p_{\mathrm{T}_{i+1}}, \tag{63b}$$

where $i = 1, \ldots, m-1$.

As shown in Fig. 1, the m^{th} link has two cutting points, one driving cutting point associated with frame $\{\mathrm{T}_{\mathrm{EE}}\}$ and one driven cutting point associated with frame $\{\mathrm{B}_m\}$; the $i^{\text{th}}, i \in [1, m-1]$, link has two cutting points, one driving cutting point associated with frame $\{\mathrm{T}_{i+1}\}$ and one driven cutting point associated with frame $\{\mathrm{B}_i\}$. Therefore, all the links are *virtually stable* in the sense of Definition 4. □

Theorem 3. *Consider the flexible joints of the manipulator described by* (10), *combined with its respective control equation* (38), *and with the parameter adaptation algorithms* (39) *and* (40). *These flexible joints are virtually stable.*

Proof. Select the nonnegative accompanying function of the i^{th} manipulator joint as

$$\begin{aligned}\nu_{\mathrm{f}i} = &\frac{1}{2}\mathcal{I}_{\mathrm{m},i}(\dot{\phi}_{\mathrm{m},i\mathrm{r}} - \dot{\phi}_{\mathrm{m},i})^2 + \frac{1}{2}\sum_{\gamma=1}^{2}\frac{\left(\theta_{\mathrm{q}i\gamma} - \hat{\theta}_{\mathrm{q}i\gamma}\right)^2}{\rho_{\mathrm{q}i\gamma}} + \\ &\frac{1}{2}\sum_{\gamma=1}^{3}\frac{\left(\theta_{\phi i\gamma} - \hat{\theta}_{\phi i\gamma}\right)^2}{\rho_{\phi i\gamma}}.\end{aligned} \tag{64}$$

When considering joint elasticity, combined with (64), the nonnegative accompanying function can be further designed as

$$\begin{aligned}\nu_{\mathrm{a}i} = &\nu_{\mathrm{f}i} + \frac{1}{2}k_{\mathrm{f},i}\left[(\phi_{\mathrm{m},i\mathrm{r}} - \phi_{\mathrm{m},i}) - (q_{\mathrm{m},i\mathrm{r}} - q_{\mathrm{m},i})\right]^2 + \\ &\frac{1}{2}(k_{\mathrm{f},i} - \hat{k}_{\mathrm{f},i})^2/\rho_{\mathrm{kf}i}.\end{aligned} \tag{65}$$

According to the third equation of (40) and Definition 2, we can obtain

$$(k_{\mathrm{f},i} - \hat{k}_{\mathrm{f},i})\left(s_{\mathrm{kf}i} - \dot{\hat{k}}_{\mathrm{f},i}/\rho_{\mathrm{kf}i}\right) \leqslant 0. \tag{66}$$

Combined with (66), the time derivative of (65) can be derived as

$$\begin{aligned}\dot{\nu}_{\mathrm{a}i} \leqslant & -k_{\mathrm{vq},i}(\dot{q}_{\mathrm{m},i\mathrm{r}} - \dot{q}_{\mathrm{m},i})^2 - k_{\mathrm{v}\phi,i}(\dot{\phi}_{\mathrm{m},i\mathrm{r}} - \dot{\phi}_{\mathrm{m},i})^2 - \\ &(\dot{q}_{\mathrm{m},i\mathrm{r}} - \dot{q}_{\mathrm{m},i})\boldsymbol{z}^{\mathrm{T}}({}^{\mathrm{B}_i}\boldsymbol{F}_{\mathrm{r}} - {}^{\mathrm{B}_i}\boldsymbol{F}).\end{aligned} \tag{67}$$

According to (4), (9), (36), (37), and Definition 3, we can derive

$$\begin{aligned}\dot{\nu}_{\mathrm{a}1} \leqslant & -k_{\mathrm{vq},1}(\dot{q}_{\mathrm{m},1\mathrm{r}} - \dot{q}_{\mathrm{m},1})^2 - k_{\mathrm{v}\phi,1}(\dot{\phi}_{\mathrm{m},1\mathrm{r}} - \dot{\phi}_{\mathrm{m},1})^2 \\ &- p_{\mathrm{B}_1} + p_{\mathrm{P}_{\mathrm{p}}},\end{aligned} \tag{68a}$$

$$\begin{aligned}\dot{\nu}_{\mathrm{a}i} \leqslant & -k_{\mathrm{vq},i}(\dot{q}_{\mathrm{m},i\mathrm{r}} - \dot{q}_{\mathrm{m},i})^2 - k_{\mathrm{v}\phi,i}(\dot{\phi}_{\mathrm{m},i\mathrm{r}} - \dot{\phi}_{\mathrm{m},i})^2 \\ &- p_{\mathrm{B}_i} + p_{\mathrm{T}_i},\ i = 2, \ldots, m.\end{aligned} \tag{68b}$$

As shown in Fig. 1, joint 1 has one driving cutting point associated with frame $\{\mathrm{B}_1\}$ and one driven cutting point associated with frame $\{\mathrm{P}_{\mathrm{p}}\}$. Joint $i, i \in [2, m]$, has two cutting points, one driving cutting point associated with frame $\{\mathrm{B}_i\}$ and one driven cutting point associated with frame $\{\mathrm{T}_i\}$. Therefore, all the flexible joints are *virtually stable* in the sense of Definition 4. □

C. Virtual Stability of Wheeled Mobile Platform

We will first prove the *virtual stability* of the MP's wheels, and followed by the *virtual stability* of the wheel joints, the MP body, and the virtual manipulator.

Theorem 4. *Consider the MP's wheels described by (12)∼(16), combined with their respective control equations (41)∼(45), and with parameter adaptation approach defined in Definition 2. Then, these wheels are virtually stable.*

Proof. Define the nonnegative accompanying function of the wheel with ID i, $i \in \{\mathrm{fl}, \mathrm{fr}, \mathrm{bl}, \mathrm{br}\}$, as

$$\nu_{\mathrm{W}_i} = \frac{1}{2}({}^{\mathrm{W}_i}\boldsymbol{V}_{\mathrm{r}} - {}^{\mathrm{W}_i}\boldsymbol{V})^{\mathrm{T}}\boldsymbol{M}_{\mathrm{W}_i}({}^{\mathrm{W}_i}\boldsymbol{V}_{\mathrm{r}} - {}^{\mathrm{W}_i}\boldsymbol{V}) + \frac{1}{2}\sum_{\gamma=1}^{13}\frac{\left(\theta_{\mathrm{W}_i\gamma} - \hat{\theta}_{\mathrm{W}_i\gamma}\right)^2}{\rho_{\mathrm{W}_i\gamma}}, \tag{69}$$

then, the time derivative of (69) can be expressed as

$$\dot{\nu}_{\mathrm{W}_i} \leqslant -({}^{\mathrm{W}_i}\boldsymbol{V}_{\mathrm{r}} - {}^{\mathrm{W}_i}\boldsymbol{V})^{\mathrm{T}}\boldsymbol{K}_{\mathrm{W}_i}({}^{\mathrm{W}_i}\boldsymbol{V}_{\mathrm{r}} - {}^{\mathrm{W}_i}\boldsymbol{V}) + p_{\mathrm{W}_i} - p_{\mathrm{C}_i}. \tag{70}$$

As shown in Fig. 2, the wheel with ID i only has one driven cutting point associated with frame $\{\mathrm{W}_i\}$. Combined with (13), (15), (42), (45), and Definitions 2 and 3, we can derive

$$\begin{aligned} p_{\mathrm{C}_i} &= (\boldsymbol{\chi}_{i,\mathrm{r}} - \boldsymbol{\chi}_i)^{\mathrm{T}}\boldsymbol{Y}_{\mathrm{c},i}(\hat{\boldsymbol{\theta}}_{\mathrm{c},i} - \boldsymbol{\theta}_{\mathrm{c},i}) \\ &= -\sum_{\gamma}(\theta_{\mathrm{c},i\gamma} - \hat{\theta}_{\mathrm{c},i\gamma})\frac{\dot{\hat{\theta}}_{\mathrm{c},i\gamma}}{\rho_{\mathrm{c},i\gamma}} - \\ &\quad \sum_{\gamma}\left\{(\theta_{\mathrm{c},i\gamma} - \hat{\theta}_{\mathrm{c},i\gamma})\left[s_{\mathrm{c},i\gamma} - \frac{\dot{\hat{\theta}}_{\mathrm{c},i\gamma}}{\rho_{\mathrm{c},i\gamma}}\right]\right\} \\ &\geqslant -\sum_{\gamma}(\theta_{\mathrm{c},i\gamma} - \hat{\theta}_{\mathrm{c},i\gamma})\frac{\dot{\hat{\theta}}_{\mathrm{c},i\gamma}}{\rho_{\mathrm{c},i\gamma}}, \end{aligned} \tag{71}$$

then, by integrating (71) with respect to time, it yields

$$\begin{aligned} \int_0^t p_{\mathrm{C}_i}\mathrm{d}\tau \geqslant & \sum_{\gamma}\frac{1}{2\rho_{\mathrm{c},i\gamma}}\left[\theta_{\mathrm{c},i\gamma} - \hat{\theta}_{\mathrm{c},i\gamma}(t)\right]^2 - \\ & \sum_{\gamma}\frac{1}{2\rho_{\mathrm{c},i\gamma}}\left[\theta_{\mathrm{c},i\gamma} - \hat{\theta}_{\mathrm{c},i\gamma}(0)\right]^2 \\ \geqslant & -\sum_{\gamma}\frac{1}{2\rho_{\mathrm{c},i\gamma}}\left[\theta_{\mathrm{c},i\gamma} - \hat{\theta}_{\mathrm{c},i\gamma}(0)\right]^2. \end{aligned} \tag{72}$$

Therefore, the MP's wheels are *virtually stable* in the sense of Definition 4. □

Theorem 5. *Consider the rigid wheel joints of the MP described by (17), combined with its respective control equation (46), and with the parameter adaptation algorithms (47) and (48). These wheel joints are virtually stable.*

Proof. Choose the nonnegative accompanying function of the wheel joint with ID i, $i \in \{\mathrm{fl}, \mathrm{fr}, \mathrm{bl}, \mathrm{br}\}$, as

$$\nu_{\mathrm{A}_i} = \frac{1}{2}\mathcal{I}_i(\omega_{i\mathrm{r}} - \omega_i)^2 + \frac{1}{2}\sum_{i=1}^{3}\frac{\left(\theta_{\mathrm{A}_i\gamma} - \hat{\theta}_{\mathrm{A}_i\gamma}\right)^2}{\rho_{\mathrm{A}_i\gamma}}, \tag{73}$$

then, the time derivative of (73) can be expressed as

$$\dot{\nu}_{\mathrm{A}_i} \leqslant -k_{\mathrm{A}_i}(\omega_{i\mathrm{r}} - \omega_i)^2 - p_{\mathrm{W}_i} + p_{\mathrm{A}_i}. \tag{74}$$

As shown in Fig. 2, the wheel joint with ID i has two cutting points, one driving cutting point associated with frame $\{\mathrm{W}_i\}$ and one driven cutting point associated with frame $\{\mathrm{A}_i\}$. Thus, all the wheel joints are *virtually stable* in the sense of Definition 4. □

Theorem 6. *Consider the MP body described by (18) and (19), combined with their respective control equations (49) and (50), and with parameter adaptation algorithms, which are the same as (32) and (33) with appropriate frame substitutions. Then, the MP body is virtually stable.*

Proof. Define the nonnegative accompanying function of the MP body $\nu_{\mathrm{P_c}}$ as

$$\nu_{\mathrm{P_c}} = \frac{1}{2}({}^{\mathrm{P_c}}\boldsymbol{V}_{\mathrm{r}} - {}^{\mathrm{P_c}}\boldsymbol{V})^{\mathrm{T}}\boldsymbol{M}_{\mathrm{P_c}}({}^{\mathrm{P_c}}\boldsymbol{V}_{\mathrm{r}} - {}^{\mathrm{P_c}}\boldsymbol{V}) + \frac{1}{2}\sum_{\gamma=1}^{13}\frac{\left(\theta_{\mathrm{P_c}\gamma} - \hat{\theta}_{\mathrm{P_c}\gamma}\right)^2}{\rho_{\mathrm{P_c}\gamma}}, \tag{75}$$

then, the time derivative of (75) can be derived as

$$\begin{aligned} \dot{\nu}_{\mathrm{P_c}} \leqslant & -({}^{\mathrm{P_c}}\boldsymbol{V}_{\mathrm{r}} - {}^{\mathrm{P_c}}\boldsymbol{V})^{\mathrm{T}}\boldsymbol{K}_{\mathrm{P_c}}({}^{\mathrm{P_c}}\boldsymbol{V}_{\mathrm{r}} - {}^{\mathrm{P_c}}\boldsymbol{V}) + \\ & p_{\mathrm{P_c}} - p_{\mathrm{P_p}} - \sum_i p_{\mathrm{A}_i}, \end{aligned} \tag{76}$$

where $i \in \{\mathrm{fl}, \mathrm{fr}, \mathrm{bl}, \mathrm{br}\}$ denotes the wheel ID.

As shown in Fig. 2, the MP body has six cutting points, five driving cutting points associated with frames $\{\mathrm{P_p}\}$, $\{\mathrm{A_{fl}}\}$, $\{\mathrm{A_{fr}}\}$, $\{\mathrm{A_{bl}}\}$, $\{\mathrm{A_{br}}\}$, respectively, and one driven cutting point associated with frame $\{\mathrm{P_c}\}$. Thus, the MP body is *virtually stable* in the sense of Definition 4. □

Theorem 7. *Consider the virtual manipulator described by ${}^{\mathrm{P_c}}\boldsymbol{F} = \boldsymbol{0}$, combined with its respective control equation (51). Then, the virtual manipulator is virtually stable.*

Proof. Define the nonnegative accompanying function of the virtual manipulator as 0, then, combined with (52), we can obtain

$$\begin{aligned} 0 &\leqslant ({}^{\mathrm{P_c}}\boldsymbol{V}_{\mathrm{r}} - {}^{\mathrm{P_c}}\boldsymbol{V})^{\mathrm{T}}\boldsymbol{K}_{\mathrm{vm}}({}^{\mathrm{P_c}}\boldsymbol{V}_{\mathrm{r}} - {}^{\mathrm{P_c}}\boldsymbol{V}) \\ &= -({}^{\mathrm{P_c}}\boldsymbol{V}_{\mathrm{r}} - {}^{\mathrm{P_c}}\boldsymbol{V})^{\mathrm{T}}({}^{\mathrm{P_c}}\boldsymbol{F}_{\mathrm{r}} - {}^{\mathrm{P_c}}\boldsymbol{F}) = -p_{\mathrm{P_c}}. \end{aligned} \tag{77}$$

As shown in Fig. 2, the virtual manipulator only has one driving cutting point associated with frame $\{\mathrm{P_c}\}$. Thus, the virtual manipulator is *virtually stable* in the sense of Definition 4. □

D. Stability of Wheeled Mobile Manipulator System

First, we will provide the following important lemmas, which play an important role in proving the L_2 and L_∞ stability of the WMM system [25].

Lemma 1. *Consider a non-negative piecewise continuous function $\xi(t)$ described as*

$$\xi(t) \geqslant \frac{1}{2}\boldsymbol{x}^{\mathrm{T}}(t)\boldsymbol{P}\boldsymbol{x}(t), \tag{78}$$

where $\boldsymbol{x}(t) \in \mathbb{R}^n$, $n \geqslant 1$, and $\boldsymbol{P} \in \mathbb{R}^{n\times n}$ is a symmetric positive-definite matrix. If the time derivative of $\xi(t)$ is Lebesgue integrable and subject to

$$\dot{\xi}(t) \leqslant -\boldsymbol{y}^{\mathrm{T}}(t)\boldsymbol{Q}\boldsymbol{y}(t) - s(t) \tag{79}$$

with $\boldsymbol{y}(t) \in \mathbb{R}^m$, $m \geqslant 1$, and $\boldsymbol{Q} \in \mathbb{R}^{m\times m}$ being a symmetric positive-definite matrix, and $s(t)$ is governed by

$$\int_0^\infty s(t)dt \geqslant -\gamma_0 \tag{80}$$

with $0 \leqslant \gamma_0 < \infty$, then it follows that $\xi(t) \in L_\infty$, $\boldsymbol{x}(t) \in L_\infty$, and $\boldsymbol{y}(t) \in L_2$ hold.

Lemma 2. *Consider a multiple-input-multiple-output first-order system described by*

$$\dot{\boldsymbol{x}}(t) + \boldsymbol{K}\boldsymbol{x}(t) = \boldsymbol{u}(t), \tag{81}$$

where $\boldsymbol{x}(t) \in \mathbb{R}^n$, $\boldsymbol{u}(t) \in \mathbb{R}^n$, and $\boldsymbol{K} \in \mathbb{R}^{n\times n}$ is a symmetrical and positive-definite matrix. If $\boldsymbol{u}(t) \in L_2 \cap L_\infty$, then, $\boldsymbol{x}(t) \in L_2 \cap L_\infty$ and $\dot{\boldsymbol{x}}(t) \in L_2 \cap L_\infty$.

Lemma 3. *Consider a multiple-input-multiple-output second-order system described by*

$$\boldsymbol{M}\ddot{\boldsymbol{x}}(t) + \boldsymbol{D}\dot{\boldsymbol{x}}(t) + \boldsymbol{K}\boldsymbol{x}(t) = \boldsymbol{u}(t), \tag{82}$$

where $\boldsymbol{x}(t) \in \mathbb{R}^n$, $\boldsymbol{u}(t) \in \mathbb{R}^n$, $\boldsymbol{M} \in \mathbb{R}^{n\times n}$, $\boldsymbol{D} \in \mathbb{R}^{n\times n}$, and $\boldsymbol{K} \in \mathbb{R}^{n\times n}$ are symmetrical and positive-definite matrices. If $\boldsymbol{u}(t) \in L_2 \cap L_\infty$, then, $\boldsymbol{x}(t) \in L_2 \cap L_\infty$ and $\dot{\boldsymbol{x}}(t) \in L_2 \cap L_\infty$.

Lemma 4. *If $e(t) \in L_2$ and $\dot{e}(t) \in L_\infty$, then, $\lim_{t\to\infty} e(t) = 0$.*

It is worth mentioning that Lemma 4 is important in demonstrating asymptotic convergence of an error signal $e(t)$.

Theorem 8. *Consider the entire WMM, which is shown in Fig. 1. If its dynamic interaction with the external environment satisfies (58) and (72). Furthermore, let the results in (57), (63), (68), (70), (74), (76), and (77) hold. Then, the stability of the WMM can be ensured.*

Proof. Select the nonnegative accompanying function of the WMM as

$$\nu = \nu_{\mathrm{EE}} + \sum_{i=1}^{m} \nu_{\mathrm{B}_i} + \sum_{i=1}^{m} \nu_{\mathrm{a}i} + \sum_{j} \nu_{\mathrm{W}_j} + \sum_{j} \nu_{\mathrm{A}_j} + \nu_{\mathrm{P_c}}, \tag{83}$$

where i and j represent the number of the manipulator joints and the ID of the MP's wheels, respectively.

According to the results in Theorems 1~7, the time derivative of (83) can be derived as

$$\begin{aligned}
\dot{\nu} \leqslant &- ({}^{\mathrm{EE}}\boldsymbol{V}_{\mathrm{r}} - {}^{\mathrm{EE}}\boldsymbol{V})^{\mathrm{T}}\boldsymbol{K}_{\mathrm{EE}}({}^{\mathrm{EE}}\boldsymbol{V}_{\mathrm{r}} - {}^{\mathrm{EE}}\boldsymbol{V}) \\
&- \sum_{i=1}^{m}({}^{\mathrm{B}_i}\boldsymbol{V}_{\mathrm{r}} - {}^{\mathrm{B}_i}\boldsymbol{V})^{\mathrm{T}}\boldsymbol{K}_{\mathrm{B}_i}({}^{\mathrm{B}_i}\boldsymbol{V}_{\mathrm{r}} - {}^{\mathrm{B}_i}\boldsymbol{V}) \\
&- ({}^{\mathrm{P_c}}\boldsymbol{V}_{\mathrm{r}} - {}^{\mathrm{P_c}}\boldsymbol{V})^{\mathrm{T}}\boldsymbol{K}_{\mathrm{P_c}}({}^{\mathrm{P_c}}\boldsymbol{V}_{\mathrm{r}} - {}^{\mathrm{P_c}}\boldsymbol{V}) \\
&- \sum_{j}({}^{\mathrm{W}_j}\boldsymbol{V}_{\mathrm{r}} - {}^{\mathrm{W}_j}V)^{\mathrm{T}}\boldsymbol{K}_{\mathrm{W}_j}({}^{\mathrm{W}_j}\boldsymbol{V}_{\mathrm{r}} - {}^{\mathrm{W}_j}\boldsymbol{V}) \\
&- \sum_{i=1}^{m}\left[k_{\mathrm{vq},i}(\dot{q}_{\mathrm{m},i\mathrm{r}} - \dot{q}_{\mathrm{m},i})^2 + k_{\mathrm{v}\phi,i}(\dot{\phi}_{\mathrm{m},i\mathrm{r}} - \dot{\phi}_{\mathrm{m},i})^2\right] \\
&- \sum_{j} k_{\mathrm{A}_j}(\omega_{j\mathrm{r}} - \omega_j)^2 - p_{\mathrm{C}} - \sum_{j} p_{\mathrm{C}_j}.
\end{aligned} \tag{84}$$

According to (58)~(60), (71)~(72), and Lemma 1, it can be concluded that

$$\begin{cases}
{}^{\mathrm{EE}}\boldsymbol{V}_{\mathrm{r}} - {}^{\mathrm{EE}}\boldsymbol{V} \in L_2 \cap L_\infty, \\
{}^{\mathrm{B}_i}\boldsymbol{V}_{\mathrm{r}} - {}^{\mathrm{B}_i}\boldsymbol{V} \in L_2 \cap L_\infty, \\
{}^{\mathrm{P}_c}\boldsymbol{V}_{\mathrm{r}} - {}^{\mathrm{P}_c}\boldsymbol{V} \in L_2 \cap L_\infty, \\
{}^{\mathrm{W}_j}\boldsymbol{V}_{\mathrm{r}} - {}^{\mathrm{W}_j}V \in L_2 \cap L_\infty, \\
\dot{q}_{\mathrm{m},i\mathrm{r}} - \dot{q}_{\mathrm{m},i} \in L_2 \cap L_\infty, \\
\dot{\phi}_{\mathrm{m},i\mathrm{r}} - \dot{\phi}_{\mathrm{m},i} \in L_2 \cap L_\infty, \\
\omega_{j\mathrm{r}} - \omega_j \in L_2 \cap L_\infty.
\end{cases} \tag{85}$$

Take the i^{th} manipulator link for example, if its required acceleration is bounded, that is, ${}^{\mathrm{B}_i}\dot{\boldsymbol{V}}_{\mathrm{r}} \in L_\infty$. Then, its required net F/T vector meets the condition ${}^{\mathrm{B}_i}\boldsymbol{F}_{\mathrm{r}}^{*} \in L_\infty$. According to these results, we can conclude that ${}^{\mathrm{B}_i}\boldsymbol{F}_{\mathrm{r}} \in L_\infty$ and $\tau_i \in L_\infty$. Further, combined with link dynamic model (9), joint dynamic model (10), and Lemmas 2 and 3, it derives ${}^{\mathrm{B}_i}\dot{\boldsymbol{V}} \in L_\infty$. Therefore, if the required acceleration of each subsystem is bounded, in line with (85) and Lemma 4, it derives

$$\begin{cases}
{}^{\mathrm{EE}}\boldsymbol{V}_{\mathrm{r}} - {}^{\mathrm{EE}}\boldsymbol{V} \to \boldsymbol{0}, \\
{}^{\mathrm{B}_i}\boldsymbol{V}_{\mathrm{r}} - {}^{\mathrm{B}_i}\boldsymbol{V} \to \boldsymbol{0}, \\
{}^{\mathrm{P}_c}\boldsymbol{V}_{\mathrm{r}} - {}^{\mathrm{P}_c}\boldsymbol{V} \to \boldsymbol{0}, \\
{}^{\mathrm{W}_j}\boldsymbol{V}_{\mathrm{r}} - {}^{\mathrm{W}_j}\boldsymbol{V} \to \boldsymbol{0}, \\
\dot{q}_{\mathrm{m},i\mathrm{r}} - \dot{q}_{\mathrm{m},i} \to 0, \\
\dot{\phi}_{\mathrm{m},i\mathrm{r}} - \dot{\phi}_{\mathrm{m},i} \to 0, \\
\omega_{j\mathrm{r}} - \omega_j \to 0.
\end{cases} \tag{86}$$

□

E. Computational Complexity Analysis

The VDC-based trajectory tracking control method proposed in this paper is an iterative algorithm, and its computational complexity significantly impacts the performance of the control system. Therefore, this subsection will focus on its discussion.

Here, we can classify the computations as follows:

(1) The computational complexity of the coefficients in the dynamic equations of the rigid body (using the end-effector as an example) and the joint (including the manipulator's flexible joint and the wheel's rigid joint) subsystems is analyzed, as represented by (8), (10), and (17), respectively.

(2) The computational complexity of the required velocities of the rigid body (using the end-effector as an example) and the joint (including the manipulator's flexible joint and the wheel's rigid joint) subsystems is analyzed, as represented by (22), (23), (24), and (35), respectively.

(3) The computational complexity of the update adaptive laws of the rigid body (using the end-effector as an example) and the joint (including the manipulator's flexible joint and the wheel's rigid joint) subsystems is analyzed, as represented by (33), (40), and (48), respectively.

(4) The computational complexity of the adaptive controllers of the rigid body (using the end-effector as an example) and the joint (including the manipulator's flexible joint and the wheel's rigid joint) subsystems is analyzed, as represented by (31), (38), and (46), respectively.

(5) The computational complexity of the external forces of the end-effector-environment and the wheel-ground subsystems is analyzed, as represented by (25), and (45), respectively.

Remark 1: In the computational complexity analysis presented above, we considered only the computations associated with a single rigid body or joint within the algorithm. The iterative processes involving velocity or force interactions between joints and links, such as those described by (36), (37), and (44), were excluded from the analysis. Nonetheless, it is evident that the computational complexity increases proportionally with the number of subsystems considered.

Remark 2: The adaptation gains in (30), (33), (40), (48), etc., are consistently treated as diagonal matrices. This assumption helps to simplify and reduce the computational burden.

Table I presents the computational complexities associated with the VDC-based adaptive control of rigid body and joint subsystems. In this context, $\bar{n}$ represents the total number of joints in the system, while r denotes the dimension of the end-effector, with $r \leqslant 6$. Accordingly, the computational costs of the multiplication and addition operations can be considered linear functions of the robot's DoFs. Furthermore, the iterative process's computational cost is also proportional to the number of DoFs. Thus, the algorithm's overall computational complexity is proportional to the number of DoFs, aligning with the findings in [38].

V. Experimental Results

Several experiments have been performed to verify the effectiveness of the proposed control approach for WMMs. Section V-A presents the experimental setup. Experimental verification of joint trajectory and EE trajectory is presented in Sections V-B and V-C, respectively. Section V-D demonstrates the performance of the proposed method in simultaneously tracking two trajectories from the MP and the EE.

A. Experimental Setup

The experiments were performed with a custom-built omnidirectional WMM, which is the sum of a 4-wheel mobile platform equipped with two pairs of Mecanum wheels and a 7-DoF ultra-lightweight robotic Gen3 arm (Kinova Robotics, Canada), as shown in Fig. 4. The Gen3 employs series elastic elements to sense joint torques. The control system operates at a frequency of 1000 Hz, corresponding to a loop period of 1 ms. It is important to note that in our experiments, the MP can only be actuated through joint velocity control rather than joint torque control. Consequently, an admittance interface is employed, as described in [50].

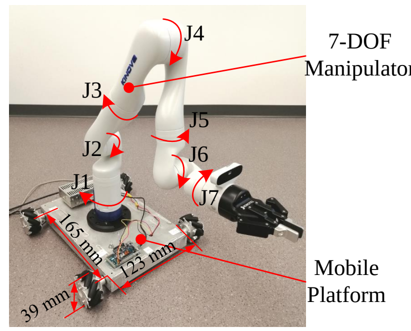

Figure 4: Experimental setup.

The admittance interface for each joint of the wheels is defined by the equation $\boldsymbol{\tau}_{\rm mp} = \boldsymbol{M}_{\rm mp}\dot{\boldsymbol{v}}_{\rm mp} + \boldsymbol{D}_{\rm mp}\boldsymbol{v}_{\rm mp}$, where $\boldsymbol{\tau}_{\rm mp} \in \mathbb{R}^{p}$ represents the resultant joint torque vector for the MP as specified in (46). The matrices $\boldsymbol{M}_{\rm mp} \in \mathbb{R}^{p\times p}$ and $\boldsymbol{D}_{\rm mp} \in \mathbb{R}^{p\times p}$ are diagonal, positive-definite matrices that represent the virtual inertia and damping of the interface, respectively. In the experimental setup, these matrices are chosen as $\boldsymbol{M}_{\rm mp} = 0.75\boldsymbol{I}_{4\times 4}$ Nm·s^2 and $\boldsymbol{D}_{\rm mp} = 2.4\boldsymbol{I}_{4\times 4}$ Nm·s. The manipulator joint stiffness coefficients, as given in (10), are sourced from Kinova Robotics and are specified as $\boldsymbol{k}_{\rm f} = [16, 16, 16, 16, 7.1, 7.1, 7.1]^{\rm T}$ kN·m/rad. Additionally, to mitigate the effect of measurement noise, a fourth-order Butterworth low-pass filter is applied to the joint acceleration, with a cutoff frequency set at 3 Hz. The control parameters implemented in the following experiments are listed in Table II. The control parameters listed in Table II are determined through trial and error during the experiments. While selecting appropriate values can achieve desirable tracking performance, excessively large values may introduce instability to the WMM. In this study, parameter sensitivity is not considered, as various parameter combinations can yield comparable tracking performance. For methods to optimize these values, readers may refer to [51]. In the experiments, the parameters were chosen such that the trajectory tracking errors remained minimal while ensuring the stable operation of the robotic system.

B. Experiment on Joint Trajectory Tracking

In this experiment, the VDC-based approach in tracking joint-space trajectories is verified. To validate the advantages of the VDC method, we conducted experimental comparisons against a PID controller, an adaptive sliding mode controller (ASMC) [52], and a neural network-based SMC (NNSMC) [53], where the nonlinearities of the robot dynamics were approximated using a NN. These approaches were selected due to their relevance in handling uncertainties and disturbances in dynamic systems. While both baseline methods were implemented with carefully tuned parameters to ensure optimal

Table I: Computational complexities of the proposed method.

Control steps	Multiplication flops	Addition flops
1. Dynamic equations denoted by (8), (10), and (17).	$72+6+3$	$72+6+3$
2. Required velocity vectors denoted by (22), (23), (24), and (35).	$6r+r^2+216+\bar{n}r^2$	$0+2r+180+\bar{n}r(r-1)$
3. Update adaptive laws denoted by (33), (40), and (48).	$470+11+5$	$6+0+0$
4. Adaptive controllers denoted by (31), (38), and (46).	$1050+14+10$	$972+16+10$
5. External forces denoted by (25), and (45).	$6r+36$	$6r+18$
Total	$(\bar{n}+1)r^2+12r+1893$	$\bar{n}r^2+(8-\bar{n})r+1283$

Table II: Control parameters adopted in the experiment.

Parameter	Value	Parameter	Value	Parameter	Value	Parameter	Value	Parameter	Value
$\boldsymbol{K}_{\mathrm{EE}}$	$3\boldsymbol{I}_{6\times 6}$	$\boldsymbol{K}_{\mathrm{B}_6}$	$3\boldsymbol{I}_{6\times 6}$	$k_{\mathrm{vq}5}$	4.5	$k_{\mathrm{v}\phi 4}$	40	$\boldsymbol{K}_{\mathrm{W_{bl}}}$	$5\boldsymbol{I}_{4\times 4}$
$\boldsymbol{K}_{\mathrm{B}_1}$	$3\boldsymbol{I}_{6\times 6}$	$\boldsymbol{K}_{\mathrm{B}_7}$	$3\boldsymbol{I}_{6\times 6}$	$k_{\mathrm{vq}6}$	4.5	$k_{\mathrm{v}\phi 5}$	40	$\boldsymbol{K}_{\mathrm{W_{br}}}$	$5\boldsymbol{I}_{4\times 4}$
$\boldsymbol{K}_{\mathrm{B}_2}$	$20\boldsymbol{I}_{6\times 6}$	$k_{\mathrm{vq}1}$	4.5	$k_{\mathrm{vq}7}$	4.5	$k_{\mathrm{v}\phi 6}$	40	$k_{\mathrm{A_{fl}}}$	8
$\boldsymbol{K}_{\mathrm{B}_3}$	$3\boldsymbol{I}_{6\times 6}$	$k_{\mathrm{vq}2}$	18	$k_{\mathrm{v}\phi 1}$	40	$k_{\mathrm{v}\phi 7}$	40	$k_{\mathrm{A_{fr}}}$	8
$\boldsymbol{K}_{\mathrm{B}_4}$	$3\boldsymbol{I}_{6\times 6}$	$k_{\mathrm{vq}3}$	4.5	$k_{\mathrm{v}\phi 2}$	200	$\boldsymbol{K}_{\mathrm{W_{fl}}}$	$5\boldsymbol{I}_{4\times 4}$	$k_{\mathrm{A_{bl}}}$	8
$\boldsymbol{K}_{\mathrm{B}_5}$	$3\boldsymbol{I}_{6\times 6}$	$k_{\mathrm{vq}4}$	4.5	$k_{\mathrm{v}\phi 3}$	40	$\boldsymbol{K}_{\mathrm{W_{fr}}}$	$5\boldsymbol{I}_{4\times 4}$	$k_{\mathrm{A_{br}}}$	8
$\boldsymbol{K}_{\mathrm{vm}}$	$12\boldsymbol{I}_{6\times 6}$	$\boldsymbol{K}_{\mathrm{P_c}}$	$6\boldsymbol{I}_{6\times 6}$						

performance, the detailed parameter configurations are omitted here for brevity. It should be noted that the baselines used in this study were adapted to the specific structure of WMMs, differing slightly from their standard forms as described in the literature. Instead, we focus on the experimental results, which demonstrate that the proposed method achieves superior trajectory tracking accuracy. Experiments were carried out using the x-axis motion of the MP and the 2$^{\mathrm{nd}}$, 4$^{\mathrm{th}}$, and 6$^{\mathrm{th}}$ joints of the manipulator as examples. The desired trajectories for each joint were defined as:

$$q_{\mathrm{d}i}(t) = q_{\mathrm{f}i}\left[\frac{t}{T} - \frac{1}{2\pi}\sin(\frac{2\pi t}{T})\right] + q_{0i}, \tag{87}$$

where $i \in \{1,5,7,9\}$ denotes the joint number, $i = 1$ represents the x-axis of the MP, and the others correspond to the joints of the manipulator; q_{0i} and $q_{\mathrm{f}i}$ denotes the initial and final positions of the i^{th} joint, respectively; and T denotes the joint motion period.

In the joint trajectory tracking experiments, the motion period was set to $T = 20$ s. The initial position for the x-axis of the MP and the manipulator joints were 0 m, $\pi/6$ rad, $\pi/2$ rad, and $-\pi/6$ rad, respectively. And the corresponding final position were 0.5 m, 0 rad, $\pi/6$ rad, and $\pi/3$ rad, respectively. The desired trajectories for the manipulator joints and the MP are illustrated in Fig. 5. Specifically, Fig. 5a shows the desired trajectories for Joint 2, Joint 4, and Joint 6, while Fig. 5b depicts the desired trajectory for the MP's motion along the x-axis.

The joint trajectory tracking performance is illustrated in Fig. 6. For the manipulator, the results are depicted in Figs. 6a–6c, while Fig. 6d presents the results for the MP. Furthermore, Table III provides the root mean square (RMS) errors obtained using the PID, ASMC, NNSMC, and the proposed VDC methods.

From the figures and Table III, it can be easily seen that the system converges to the desired trajectories and achieves good steady-state tracking performances by using the proposed VDC scheme. Using the PID method, the maximum tracking errors for Joint 2, Joint 4, Joint 6, and x-axis motion were

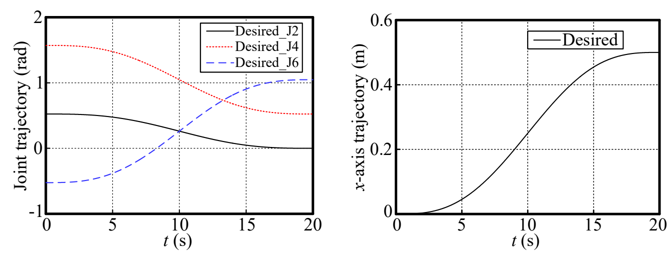

(a) Manipulator trajectory (b) MP trajectory

Figure 5: The desired trajectory of the tested manipulator joints and the MP.

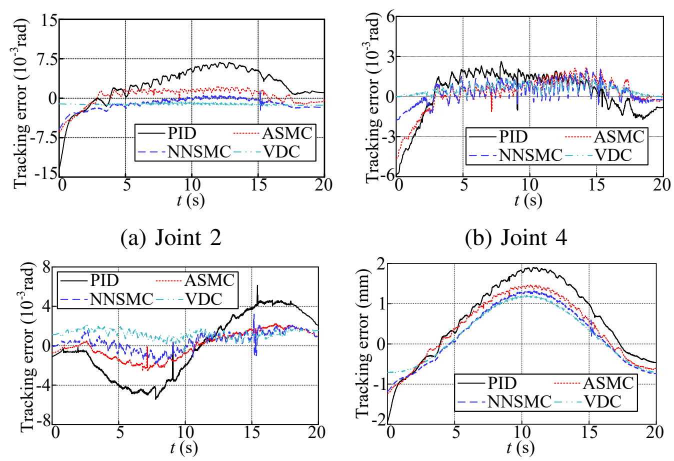

(a) Joint 2 (b) Joint 4

(c) Joint 6 (d) x-axis motion

Figure 6: Experimental results of WMM's joint trajectory tracking.

1.35×10^{-2} rad, 5.9×10^{-3} rad, 6.1×10^{-3} rad, and 1.95 mm, respectively. In contrast, with the proposed VDC method, the maximum tracking errors were reduced to 1.5×10^{-3} rad, 1.8×10^{-3} rad, 2.1×10^{-3} rad, and 1.22 mm, accounting for only 11.1%, 30.5%, 34.4%, and 62.6% of the errors observed with PID control. Additionally, the RMS error results

Table III: Comparison of RMS errors in joint trajectory tracking.

Methods	Joint 2 (rad)	Joint 4 (rad)	Joint 6 (rad)	x-axis (mm)
PID	4.2×10^{-3}	1.8×10^{-3}	3.2×10^{-3}	1.13
ASMC	1.7×10^{-3}	1.3×10^{-3}	1.4×10^{-3}	0.88
NNSMC	1.6×10^{-3}	8×10^{-4}	1.0×10^{-3}	0.79
VDC	1.2×10^{-3}	7×10^{-4}	9×10^{-4}	0.71

in Table III further demonstrate that the proposed VDC method outperformed the other three comparison methods in terms of tracking performance. These experimental findings clearly highlight that the proposed adaptive control method based on VDC offers significantly superior joint trajectory tracking performance compared to the PID and ASMC methods. This improvement stems from the incorporation of the system's nominal model into the VDC scheme, which enables online parameter adjustments based on the tracking error output.

C. Experiment on End-Effector Trajectory Tracking

The performance of the proposed approach in tracking an EE trajectory is verified in this section. Here, we selected the NNSMC method, which demonstrated strong performance in Section V-B, as a baseline for comparison to validate the advantages of the VDC method in tracking the EE trajectory of the WMM. Define the required EE trajectory as $\boldsymbol{x}_{\mathrm{ee,r}}(t) = \boldsymbol{x}_{\mathrm{ee0}} + [0, R_{\mathrm{ee}} \sin(\pi/15t), R_{\mathrm{ee}}/2 \sin(2\pi/15t)]^{\mathrm{T}}$ with $R_{\mathrm{ee}} = 0.2$ m, where $\boldsymbol{x}_{\mathrm{ee0}}$ denotes the initial position of the EE. In the subsequent task-space trajectory tracking experiments, the initial generalized coordinate vector of the WMM is denoted as $\boldsymbol{q}_0 = [0, 0, 0, 0, \pi/6, 0, \pi/2, 0, -\pi/6, 0]^{\mathrm{T}}$, where the first three parameters correspond to the MP. Using the WMM forward kinematics, the initial positions of both the EE and the MP are derived and represented as $\boldsymbol{x}_{\mathrm{ee0}} = [0.8435, -0.0246, 0.4921]^{\mathrm{T}}$ m and $\boldsymbol{x}_{\mathrm{mp0}} = [0, 0]^{\mathrm{T}}$ m. The experimental results are shown in Figs. 7 and 8. Here, Figs. 7b and 7c respectively show the configurations of the WMM at the positive y-axis limit and the negative y-axis limit.

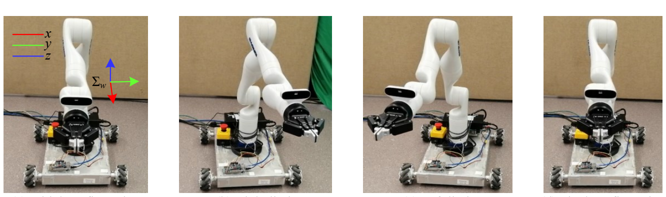

(a) Initial configuration (b) Right limit (c) Left limit (d) Final configuration

Figure 7: Sequence diagram of EE's motion process.

Fig. 8a illustrates the trajectory of the EE. As the desired trajectory lay in the $y - z$ plane of the world frame, the x-axis trajectory was not provided. From Fig. 8b, the maximum tracking errors in the y and z directions based on the NNSMC method were 2.01 mm and 4.82 mm, respectively, while the corresponding errors using the proposed VDC method were reduced to 1.51 mm and 3.02 mm, representing decreases of 24.9% and 37.3%, respectively. This result strongly demonstrates the effectiveness of the VDC-based adaptive

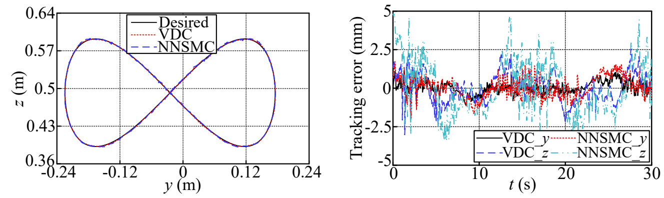

(a) EE trajectory (b) Tracking error

Figure 8: Trajectory tracking results of the EE.

method in tracking an task-space trajectory. This conclusion is expected because the desired end-effector trajectory was calculated through inverse kinematics to obtain the desired joint trajectories, which were then sent to the WMM.

D. Experiment on Dual Trajectory Tracking

As demonstrated in (86), a key strength of the proposed approach is its ability to guarantee trajectory tracking stability in both joint space and task space. This capability is of great importance in controlling multi-DoF robots, including redundant robotic systems.

In this study, we designed a dual-trajectory tracking framework for redundant WMM systems using a task-priority-based redundancy resolution approach. Unlike the method in (35), this framework simultaneously tracks two task-space trajectories by utilizing the redundancy of the robotic system: one for the EE and the other for the MP, with priority assigned to the EE. It is noteworthy that this method merely employs a different approach to generate the required joint velocity vector for the WMM, and thus does not affect the system's stability.

Here, the dual-trajectory tracking approach is designed as $\boldsymbol{v}_{\mathrm{r}} = \boldsymbol{J}^{\dagger}\dot{\boldsymbol{x}}_{\mathrm{ee,r}} + \boldsymbol{\mathcal{N}}_1(\boldsymbol{J}_2\boldsymbol{\mathcal{N}}_1)^{\dagger}(\dot{\boldsymbol{x}}_{\mathrm{mp,r}} - \boldsymbol{J}_2\boldsymbol{J}^{\dagger}\dot{\boldsymbol{x}}_{\mathrm{ee,r}})$, where $\dot{\boldsymbol{x}}_{\mathrm{ee,r}}$ represents the required EE's velocity, $\dot{\boldsymbol{x}}_{\mathrm{mp,r}}$ denotes the required MP's velocity. The matrix $\boldsymbol{\mathcal{N}}_1 = \boldsymbol{I} - \boldsymbol{J}^{\dagger}\boldsymbol{J}$ represents the orthogonal projector in the $\boldsymbol{J}$'s null space, $\boldsymbol{J}_2$ is the extended Jacobian of the MP for the following controller design. For additional details, please refer to our previous research [10].

Two scenarios with trajectories of different scales for the EE and the MP are considered. The first scenario is both two trajectories can be tracked. The second scenario is to track the EE trajectory at the expense of the MP trajectory tracking accuracy. To further analyze the performance of the controller, we defined three performance indexes to verify the quality of the proposed control. (1) $e_{\mathrm{M}} = \max_{0 \leq t \leq T} |e(t)|$: The maximum absolute tracking error for the WMM, which can be viewed as a measure of the worst tracking accuracy. (2) $L_1[e] = (1/T)\int_0^T |e| dt$: The integral mean of the tracking error for the WMM. (3) $L_2[e] = \left((1/T)\int_0^T |e|^2 dt\right)^{1/2}$: The RMS of the tracking error for the WMM. In the above indexes, e denotes the tracking error and T represents the entire running time.

The desired trajectories are defined as follows: for the EE, $\boldsymbol{x}_{\mathrm{ee,r}}(t) = \boldsymbol{x}_{\mathrm{ee0}} + [R_{\mathrm{ee}} \sin(\pi/10t), -R_{\mathrm{ee}}/2 \sin(\pi/5t), 0]^{\mathrm{T}}$, and for the MP, $\boldsymbol{x}_{\mathrm{mp,r}}(t) = \boldsymbol{x}_{\mathrm{mp0}} + [-R_{\mathrm{mp}} \cos(\pi/10t) +$

Table IV: The performance indexes of the WMM.

		x-direction (mm)			y-direction (mm)		
		e_{M}	$L_1[e]$	$L_2[e]$	e_{M}	$L_1[e]$	$L_2[e]$
Scenario 1	EE	2.56	0.65	0.77	1.08	0.42	0.48
	MP	1.89	1.06	1.13	1.57	0.75	0.83
Scenario 2	EE	4.74	0.64	0.99	0.95	0.32	0.39
	MP	257.05	82.79	128.83	41.49	9.05	16.08

$R_{\mathrm{mp}}, -R_{\mathrm{mp}} \sin(\pi/10t)]^{\mathrm{T}}$. The trajectory parameters for the two scenarios are as follows: **Scenario 1:** $R_{\mathrm{ee}} = 0.2\,\mathrm{m}$, $R_{\mathrm{mp}} = 0.2\,\mathrm{m}$; **Scenario 2:** $R_{\mathrm{ee}} = 0.2\,\mathrm{m}$, $R_{\mathrm{mp}} = -0.2\,\mathrm{m}$. Table IV shows the control performance of the proposed approach in the two scenarios.

The experimental results of **Scenario 1** are shown in Table IV and Figs. 9-12. It is obvious that in this scenario, both of the EE and MP trajectories could be tracked. Notably, the desired trajectory for the EE is confined to the $x-y$ plane, and thus, tracking results for the z direction are not provided.

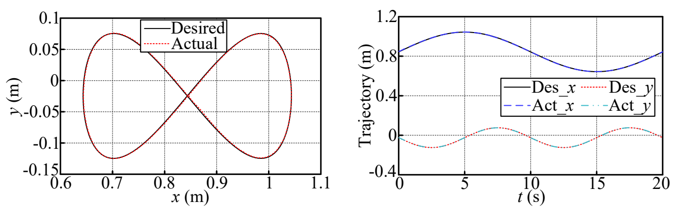

(a) Trajectory on $x-y$ plane (b) Trajectory w.r.t. time

Figure 9: Trajectory of the EE in **Scenario 1**.

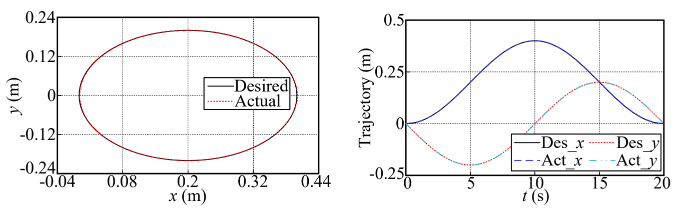

(a) Trajectory on $x-y$ plane (b) Trajectory w.r.t. time

Figure 10: Trajectory of the MP in **Scenario 1**.

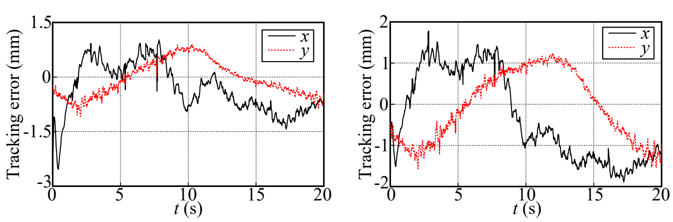

(a) Tracking error of the EE (b) Tracking error of the MP

Figure 11: Tracking error of the WMM in **Scenario 1**.

The trajectory tracking results of the EE in this scenario are shown in Figs. 9 and 11a. An "8"-shaped trajectory was provided for the EE. The maximum tracking error occurred at 0.39 s in the x-direction, measuring 2.56 mm, which corresponded to 0.64% of its total motion range. The $L_2[e]$

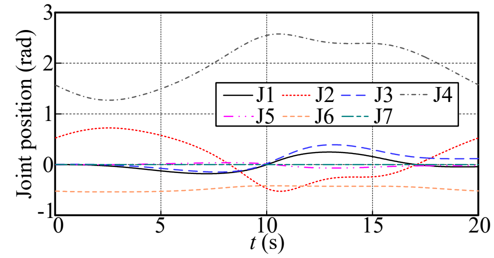

Figure 12: Joint position of the WMM in **Scenario 1**.

values of the tracking errors in the x-axis and y-axis were 0.77 mm and 0.48 mm, respectively. These values accounted for only 0.19% and 0.21% of their respective displacements.

The trajectory tracking results of the MP are shown in Figs. 10 and 11b. In contrast to the EE, the desired trajectory for the MP was a circle with a radius of 0.2 m. The x-axis exhibited the maximum tracking error, which was 1.89 mm, , accounting for no more than 0.47% of the displacement in the corresponding direction. The $L_1[e]$ values of the tracking errors reached their maximum in the x-direction, but this was only about 0.27% of the total displacement.

The joint position of the manipulator in the experiment is presented in Fig. 12. It is evident that during the dual trajectory tracking process of the EE and the MP, the movement of the manipulator's joints was smooth, with no abrupt changes in position.

Based on the experimental results, it can be concluded that when the trajectories of the EE and the MP did not interfere with each other, the proposed dynamic control method based on VDC effectively tracked both trajectories without compromising the stability at the joint level of the entire system.

The experimental results of **Scenario 2** are shown in Table IV and Figs. 13-16. Under this scenario, due to the workspace limitations of the WMM, the desired trajectories of the EE and MP could not be simultaneously satisfied. Here, the designed dual-trajectory tracking approach was employed, prioritizing the EE trajectory tracking.

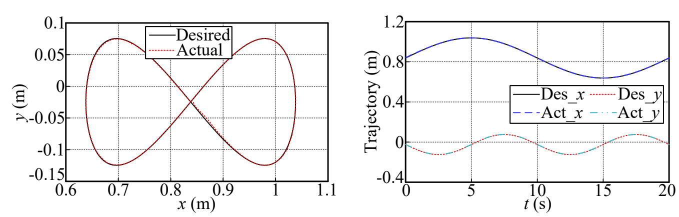

(a) Trajectory on $x-y$ plane (b) Trajectory w.r.t. time

Figure 13: Trajectory of the EE in **Scenario 2**.

Figs. 13 and 15a present the tracking error of the EE. An "8"-shaped trajectory, identical to that in **Scenario 1**, was set for the EE. The maximum tracking error, which was 4.74 mm and corresponded to 1.19% of the total motion range, occurred in the x-direction, while the $L_2[e]$ values in both axes remained below 1 mm.

The experimental results of the MP are shown in Figs. 14 and 15b. Here, the maximum tracking errors were 257.05 mm

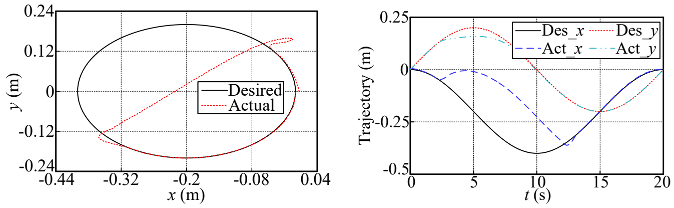

(a) Trajectory on $x-y$ plane (b) Trajectory w.r.t. time

Figure 14: Trajectory of the MP in **Scenario 2**.

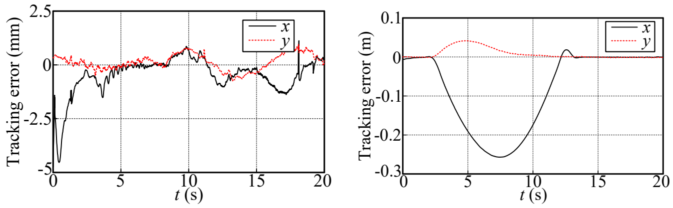

(a) Tracking error of the EE (b) Tracking error of the MP

Figure 15: Tracking error of the WMM in **Scenario 2**.

in the x-axis and 41.49 mm in the y-axis, which correspond to 64.26% and 20.75% of their respective motion ranges. These values significantly exceed the acceptable error limits for trajectory tracking. It should be noted, however, that these errors arose from the inability of the EE and MP to track both trajectories simultaneously and were due to the task prioritization setup. They were unavoidable errors and not a result of the adaptive controller proposed in this study.

The joint position curves of the manipulator under this scenario are shown in Fig. 16. As with **Scenario 1**, the joint position variations of the manipulator remained smooth, which demonstrated that the proposed trajectory tracking method maintained joint movement stability even when the EE and MP trajectories could not be tracked simultaneously.

In addition, during the experiment, we measured the time required for a single control loop. On the experimental hardware used, the average duration of a single loop was approximately 0.78 ms, meeting the real-time requirements of the experiment.

Although the experimental results demonstrate the effectiveness of the proposed method, certain aspects require further refinement for real-time applications. The VDC-based algorithm, which incorporates the full nonlinear dynamics of the WMM, can impose a substantial computational burden on systems with limited onboard processing power, highlighting

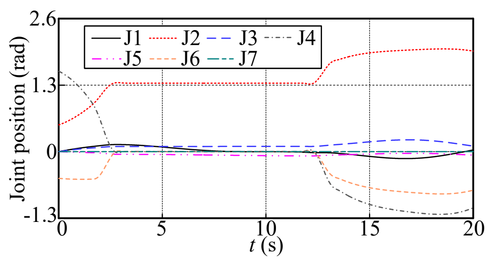

Figure 16: Joint position of the WMM in **Scenario 2**.

the need for optimization techniques such as real-time efficient solvers. Mechanical constraints, including joint elasticity, friction, and wheel-ground interactions, also affect system behavior. While these factors are considered in the control framework to enhance robustness, extreme conditions like severe terrain unevenness or high joint compliance may demand additional parameter tuning. Electrical challenges, such as actuator saturation and sensor noise, are common in real-world systems. Although the control approach adaptively addresses external disturbances, sudden power interruptions or excessive noise may still impact performance, requiring hardware-level solutions. Environmental factors, such as uneven terrain, dust, and moisture, pose further challenges by affecting stability, wheel-ground interactions, and sensor reliability. While the framework is robust against moderate disturbances, extreme conditions may necessitate measures like sensor sealing and dynamic terrain adaptation strategies to ensure reliable operation.

VI. Conclusions

In this paper, we present a novel trajectory tracking control method in Cartesian space for wheeled mobile manipulators (WMMs). To achieve high-bandwidth closed-loop performance, the internal control of the WMM was designed using the subsystem-dynamics-based virtual decomposition control (VDC) approach. This design explicitly accounts for the manipulator's joint flexibility and external disturbances, significantly enhancing trajectory tracking accuracy. The L_2 and L_∞ stability of the proposed VDC-based controller is rigorously proven for both the subsystems and the overall WMM. Additionally, the asymptotic convergence of the joints' and end-effector's trajectory tracking has been proved.

The effectiveness of the proposed approach was experimentally proven on a custom-built WMM, and comparative experiments were conducted with three different methods. The proposed method demonstrated high accuracy for joint trajectory tracking, with a maximum tracking error not exceeding 2.1×10^{-3} rad. The maximum tracking error of the proposed method for end-effector trajectory tracking was approximately 3.02 mm. In the case of dual-trajectory tracking for both the end-effector and the mobile platform, when the given trajectories were compatible with the redundancy of the WMM, the RMS tracking errors were limited to 0.77 mm for the end-effector and 1.13 mm for the mobile platform.

While this study focuses on WMMs, the developed VDC-based control approach is extendable to systems involving other robotic configurations. Its ability to rigorously address nonlinear dynamic behavior makes it applicable to dynamically complex tasks, such as bipedal locomotion and manipulation under constrained conditions.

Despite the promising results, certain limitations exist in the current study. (1) Theoretical Limitations: The analysis assumes ideal sensor feedback, which may not hold under uncertainties and noise. Additionally, the model does not address the identification of external disturbances, such as dynamic loads, which are frequently encountered in real-world applications. (2) Practical Limitations: Experiments were conducted in structured, static environments on a custom-built

WMM. Performance in dynamic, unstructured terrains and under payload variations remains untested.

Our future work will focus on enhancing the control framework's robustness to uncertainties, unmodeled dynamics, and external disturbances. We will explore its scalability to systems with reduced redundancy or increased complexity. Practical validation will be extended to dynamic and unstructured environments, with the integration of advanced state estimation and sensor fusion techniques. By addressing these limitations, the proposed approach has the potential to evolve into a robust control framework applicable to a wide range of robotic systems, including aerospace, industrial automation, and bipedal locomotion.

References

[1] K. Bussmann, A. Dietrich, and C. Ott, "Whole-body impedance control for a planetary rover with robotic arm: Theory, control design, and experimental validation," in *IEEE International Conference on Robotics and Automation (ICRA)*. IEEE, 2018, pp. 910–917.

[2] H. Xing, K. Xia, L. Ding, H. Gao, G. Liu, and Z. Deng, "Unknown geometrical constraints estimation and trajectory planning for robotic door-opening task with visual teleoperation assists," *Assembly Automation*, vol. 39, no. 3, pp. 479–488, 2019.

[3] P. Štibinger, G. Broughton, F. Majer, Z. Rozsypálek, A. Wang, K. Jindal, A. Zhou, D. Thakur, G. Loianno, T. Krajník *et al.*, "Mobile manipulator for autonomous localization, grasping and precise placement of construction material in a semi-structured environment," *IEEE Robotics and Automation Letters*, vol. 6, no. 2, pp. 2595–2602, 2021.

[4] H. Xing, A. Torabi, L. Ding, H. Gao, Z. Deng, V. K. Mushahwar, and M. Tavakoli, "An admittance-controlled wheeled mobile manipulator for mobility assistance: Human–robot interaction estimation and redundancy resolution for enhanced force exertion ability," *Mechatronics*, vol. 74, p. 102497, 2021.

[5] V. Padois, J.-Y. Fourquet, and P. Chiron, "Kinematic and dynamic model based control of wheeled mobile manipulators: a unified framework for reactive approaches," *Robotica*, vol. 25, no. 2, pp. 157–173, 2007.

[6] X. Xu, H. Xie, C. Wang, and H. Yang, "Kinematic and dynamic models of hyper -redundant manipulator based on link eigenvectors," *IEEE/ASME Transactions on Mechatronics*, vol. 29, no. 2, pp. 1306–1318, 2024.

[7] H. G. Tanner and K. J. Kyriakopoulos, "Mobile manipulator modeling with kane's approach," *Robotica*, vol. 19, no. 6, pp. 675–690, 2001.

[8] J. Peng, Z. Yang, Y. Wang, F. Zhang, and Y. Liu, "Robust adaptive motion/force control scheme for crawler-type mobile manipulator with nonholonomic constraint based on sliding mode control approach," *ISA Transactions*, vol. 92, pp. 166–179, 2019.

[9] X. Ren, Y. Liu, Y. Hu, and Z. Li, "Integrated task sensing and whole body control for mobile manipulation with series elastic actuators," *IEEE Transactions on Automation Science and Engineering*, vol. 20, no. 1, pp. 413–424, 2023.

[10] H. Xing, L. Ding, H. Gao, W. Li, and M. Tavakoli, "Dual-user haptic teleoperation of complementary motions of a redundant wheeled mobile manipulator considering task priority," *IEEE Transactions on Systems, Man, and Cybernetics: Systems*, vol. 52, no. 10, pp. 6283–6295, 2022.

[11] H. Seraji, "A unified approach to motion control of mobile manipulators," *The International Journal of Robotics Research*, vol. 17, no. 2, pp. 107–118, 1998.

[12] G. Picard, R. Lenain, Y. Mezouar, B. Thuilot, and J. Laneurit, "Multi-trajectory approach for a generic coordination paradigm of wheeled mobile manipulators," *IEEE Robotics and Automation Letters*, vol. 7, no. 2, pp. 2329–2336, 2022.

[13] A. De Luca, G. Oriolo, and P. R. Giordano, "Kinematic modeling and redundancy resolution for nonholonomic mobile manipulators," in *IEEE International Conference on Robotics and Automation*. IEEE, 2006, pp. 1867–1873.

[14] F. Chen, M. Selvaggio, and D. G. Caldwell, "Dexterous grasping by manipulability selection for mobile manipulator with visual guidance," *IEEE Transactions on Industrial Informatics*, vol. 15, no. 2, pp. 1202–1210, 2019.

[15] H. Xing, Z. Gong, L. Ding, A. Torabi, J. Chen, H. Gao, and M. Tavakoli, "An adaptive multi-objective motion distribution framework for wheeled mobile manipulators via null-space exploration," *Mechatronics*, vol. 90, p. 102949, 2023.

[16] D. Naderi, A. Meghdari, and M. Durali, "Dynamic modeling and analysis of a two DOF mobile manipulator," in *International Design Engineering Technical Conferences and Computers and Information in Engineering Conference*. American Society of Mechanical Engineers, 2000, pp. 1025–1033.

[17] H. G. Tanner and K. J. Kyriakopoulos, "Mobile manipulator modeling with Kane's approach," *Robotica*, vol. 19, no. 6, pp. 675–690, 2001.

[18] Y. Liu and Y. Li, "Dynamic modeling and adaptive neural-fuzzy control for nonholonomic mobile manipulators moving on a slope," *International Journal of Control, Automation, and Systems*, vol. 4, no. 2, pp. 197–203, 2006.

[19] A. H. Khan, S. Li, D. Chen, and L. Liao, "Tracking control of redundant mobile manipulator: An RNN based metaheuristic approach," *Neurocomputing*, vol. 400, pp. 272–284, 2020.

[20] M. Rani, N. Kumar, and H. P. Singh, "Force/motion control of constrained mobile manipulators including actuator dynamics," *International Journal of Dynamics and Control*, vol. 7, no. 3, pp. 940–954, 2019.

[21] Z. Li, T. Zhao, F. Chen, Y. Hu, C.-Y. Su, and T. Fukuda, "Reinforcement learning of manipulation and grasping using dynamical movement primitives for a humanoidlike mobile manipulator," *IEEE/ASME Transactions on Mechatronics*, vol. 23, no. 1, pp. 121–131, 2017.

[22] F. Ghorbel, J. Hung, and M. Spong, "Adaptive control of flexible-joint manipulators," *IEEE Control Systems Magazine*, vol. 9, no. 7, pp. 9–13, 1989.

[23] M. M. Fateh, "Robust control of flexible-joint robots using voltage control strategy," *Nonlinear Dynamics*, vol. 67, no. 2, pp. 1525–1537, 2012.

[24] H. Ma, Q. Zhou, H. Li, and R. Lu, "Adaptive prescribed performance control of a flexible-joint robotic manipulator with dynamic uncertainties," *IEEE Transactions on Cybernetics*, vol. 52, no. 12, pp. 12 905–12 915, 2022.

[25] L. Ding, H. Xing, H. Gao, A. Torabi, W. Li, and M. Tavakoli, "VDC-based admittance control of multi-DOF manipulators considering joint flexibility via hierarchical control framework," *Control Engineering Practice*, vol. 124, p. 105186, 2022.

[26] M. J. Kim, F. Beck, C. Ott, and A. Albu-Schäffer, "Model-free friction observers for flexible joint robots with torque measurements," *IEEE Transactions on Robotics*, vol. 35, no. 6, pp. 1508–1515, 2019.

[27] S. Zhang, Y. Wu, X. He, and Z. Liu, "Cooperative fault-tolerant control for a mobile dual flexible manipulator with output constraints," *IEEE Transactions on Automation Science and Engineering*, vol. 19, no. 4, pp. 2689–2698, 2022.

[28] Q. Du, C. Song, W. Ding, L. Zhao, and Y. Luo, "Vibration suppression method of humanoid flexible arm based on model-free predictive control," *Advanced Robotics*, vol. 35, no. 7, pp. 450–458, 2021.

[29] Z. Du, X. Xie, Z. Qu, Y. Hu, and V. Stojanovic, "Dynamic event-triggered consensus control for interval type-2 fuzzy multi-agent systems," *IEEE Transactions on Circuits and Systems I: Regular Papers*, vol. 71, no. 8, pp. 3857–3866, 2024.

[30] E. Papadopoulos and J. Poulakakis, "Planning and model-based control for mobile manipulators," in *IEEE/RSJ International Conference on Intelligent Robots and Systems*. IEEE, 2000, pp. 1810–1815.

[31] R. Fareh, M. R. Saad, M. Saad, A. Brahmi, and M. Bettayeb, "Trajectory tracking and stability analysis for mobile manipulators based on decentralized control," *Robotica*, vol. 37, no. 10, pp. 1732–1749, 2019.

[32] Y. Yamamoto and X. Yun, "Effect of the dynamic interaction on coordinated control of mobile manipulators," *IEEE Transactions on Robotics and Automation*, vol. 12, no. 5, pp. 816–824, 1996.

[33] M. Galicki, "An adaptive non-linear constraint control of mobile manipulators," *Mechanism and Machine Theory*, vol. 88, pp. 63–85, 2015.

[34] Q. Zhang, X. Song, S. Song, and V. Stojanovic, "Finite-time sliding mode control for singularly perturbed pde systems," *Journal of the Franklin Institute*, vol. 360, no. 2, pp. 841–861, 2023.

[35] X. Song, C. Wu, V. Stojanovic, and S. Song, "1 bit encoding–decoding-based event-triggered fixed-time adaptive control for unmanned surface vehicle with guaranteed tracking performance," *Control Engineering Practice*, vol. 135, p. 105513, 2023.

[36] X. Wang, D. Wang, M. Du, K. Song, Y. Ni, and Y. Li, "A two-layer trajectory tracking control scheme of manipulator based on elm-smc for autonomous robotic vehicle," *IEEE Transactions on Automation Science and Engineering*, vol. 21, no. 3, pp. 2337–2348, 2024.

[37] M. Habibnejad Korayem, N. Ghobadi, and S. Fathollahi Dehkordi, "Designing an optimal control strategy for a mobile manipulator and its application by considering the effect of uncertainties and wheel slipping," *Optimal Control Applications and Methods*, vol. 42, no. 5, pp. 1487–1511, 2021.

[38] W.-H. Zhu, *Virtual Decomposition Control - Toward Hyper Degrees of Freedom Robots*. Springer Science & Business Media, 2010.

[39] H. F. Al-Shuka, B. Corves, and W.-H. Zhu, "Function approximation technique-based adaptive virtual decomposition control for a serial-chain manipulator," *Robotica*, vol. 32, no. 3, pp. 375–399, 2014.

[40] M. Jafarinasab, S. Sirouspour, and E. Dyer, "Model-based motion control of a robotic manipulator with a flying multirotor base," *IEEE/ASME Transactions on Mechatronics*, vol. 24, no. 5, pp. 2328–2340, 2019.

[41] C. O. Luna, M. H. Rahman, M. Saad, P. Archambault, and W.-H. Zhu, "Virtual decomposition control of an exoskeleton robot arm," *Robotica*, vol. 34, no. 7, pp. 1587–1609, 2016.

[42] K. Xia, H. Xing, L. Ding, H. Gao, G. Liu, and Z. Deng, "Virtual decomposition based modeling for multi-DOF manipulator with flexible joint," *IEEE Access*, vol. 7, pp. 91 582–91 592, 2019.

[43] J. Koivumäki and J. Mattila, "Stability-guaranteed impedance control of hydraulic robotic manipulators," *IEEE/ASME Transactions on Mechatronics*, vol. 22, no. 2, pp. 601–612, 2017.

[44] A. Brahmi, M. Saad, G. Gauthier, W.-H. Zhu, and J. Ghommam, "Adaptive control of multiple mobile manipulators transporting a rigid object," *International Journal of Control, Automation and Systems*, vol. 15, pp. 1779–1789, 2017.

[45] M. Sun, X. Ouyang, J. Mattila, Z. Chen, H. Yang, and H. Liu, "Lightweight electrohydrostatic actuator drive solution for exoskeleton robots," *IEEE/ASME Transactions on Mechatronics*, vol. 27, no. 6, pp. 4631–4642, 2022.

[46] L. Sciavicco and B. Siciliano, *Modelling and control of robot manipulators*. Springer Science & Business Media, 2012.

[47] G. D. White, R. M. Bhatt, C. P. Tang, and V. N. Krovi, "Experimental evaluation of dynamic redundancy resolution in a nonholonomic wheeled mobile manipulator," *IEEE/ASME Transactions on Mechatronics*, vol. 14, no. 3, pp. 349–357, 2009.

[48] T. Ren, Y. Dong, D. Wu, and K. Chen, "Collision detection and identification for robot manipulators based on extended state observer," *Control Engineering Practice*, vol. 79, pp. 144–153, 2018.

[49] X. Liu, F. Zhao, S. S. Ge, Y. Wu, and X. Mei, "End-effector force estimation for flexible-joint robots with global friction approximation using neural networks," *IEEE Transactions on Industrial Informatics*, vol. 15, no. 3, pp. 1730–1741, 2019.

[50] A. Dietrich, K. Bussmann, F. Petit, P. Kotyczka, C. Ott, B. Lohmann, and A. Albu-Schäffer, "Whole-body impedance control of wheeled mobile manipulators," *Autonomous Robots*, vol. 40, no. 3, pp. 505–517, 2016.

[51] J.-J. Slotine and L. Weiping, "Adaptive manipulator control: A case study," *IEEE Transactions on Automatic Control*, vol. 33, no. 11, pp. 995–1003, 1988.

[52] J. Baek, M. Jin, and S. Han, "A new adaptive sliding-mode control scheme for application to robot manipulators," *IEEE Transactions on industrial electronics*, vol. 63, no. 6, pp. 3628–3637, 2016.

[53] Ruchika and N. Kumar, "Finite time control scheme for robot manipulators using fast terminal sliding mode control and rbfnn," *International Journal of Dynamics and Control*, vol. 7, pp. 758–766, 2019.